Title
GaSb-based Infrared Detectors on GaAs Substrates using an Interfacial Misfit Array

Author
Reyner, Charles

Publication Date
2013

UNIVERSITY OF CALIFORNIA

Los Angeles

GaSb-based Infrared Detectors on GaAs Substrates using an Interfacial Misfit Array

A dissertation submitted in partial satisfaction of the

requirements for the degree Doctor of Philosophy

in Electrical Engineering

by

Charles Reyner

2013

ABSTRACT OF THE DISSERTATION

GaSb-based Infrared Detectors on GaAs Substrates using

an Interfacial Misfit Array

by

Charles Reyner

Doctor of Electrical Engineering

University of California, Los Angeles, 2013

Professor Diana L. Huffaker, Chair

Infrared detectors based on compound semiconductor technology are on the verge of outperforming HgCdTe, the leading infrared material for the past 50 years. The driving force behind this change has been the development of new detector designs based on the 6.1 Å lattice constant, which includes GaSb, AlSb, and InAs binary materials. While the epitaxial deposition of these materials on GaSb substrates has enabled high performance devices, key limitations still exist. The lack of a large diameter, semi-insulating substrate; a mature, ohmic *n*-contact to GaSb; and a low *k*, large bandgap material for avalanche multiplication are all key weaknesses of this material system that further limit device development.

These challenges can be met by the introduction of a new epitaxial growth mode. The growth mode, an interfacial misfit array (IMF), enables the epitaxial deposition of a high quality, relaxed GaSb epilayer on a GaAs substrate without the creation of residual threading dislocations. The IMF achieves this feat through the creation of a 90° dislocation network at the GaSb/GaAs interface, i.e. a gallium dangling bond every 14 GaAs lattice sites.

In this dissertation, the structural, electrical, and optical characterization of IMF-based material and devices are all described. X-ray diffraction experiments are used to show that the dislocation

network is nearly perfectly correlated, i.e. there is a 99% correlation between the location of one Lomer dislocation in the IMF network and its adjacent dislocations. Further evidence is given that the material is over 99.5% relaxed after 250 nm of growth, and continues to relax as the GaSb epilayer becomes thicker. Optical RF measurements of GaSb *p-i-n* homojunctions on GaAs semi-insulating substrates show that the IMF is capable of passing high frequency signals, and that the background acceptor concentration can be reduced to approximately 2 x 10^{16} cm^{-3} using Tellurium compensation doping. *C-V* profiles of one-sided GaAs junctions indicate that the gallium dangling bonds at the IMF interface do behave as acceptors, but that the interface charge density is 1.8 x 10^{12} cm^{-2}, as opposed to the Lomer dislocation density of 3 x 10^{12} cm^{-2}. And finally, avalanche photodiodes using the IMF interface charge are utilized to create gain in 1.55 µm detectors, with both GaAs and AlGaAs multiplication regions. Low ionization coefficient ratios between holes and electrons (*k* values) of 0.1-0.4 are measured, indicating that the ultimate gain bandwidth product for IMF-based devices is several hundred GHz. Delta-doping is also shown to improve the optical response of the devices, without impacting the breakdown voltage or creating a commensurate increase in dark current. In short, IMF-based materials can meet the next challenges awaiting the 6.1 Å material system.

The dissertation of Charles Reyner is approved.

Robert N. Candler

Mark S. Goorsky

Dwight C. Streit

Diana L. Huffaker, Committee Chair

University of California, Los Angeles

2013

Table of Contents

Acknowledgments vii
Vita viii
Publications ix
Chapter 1: Introduction 1
Chapter 2: Literature Review 4
1. Overview of Molecular Beam Epitaxy 4
2. Lattice-Mismatched Semiconductors 5
2.1. Selective Area Epitaxy 6
2.2. Wafer Bonding 7
2.3. Metamorphic Buffers 9
2.4. Interfacial Misfit Arrays 10
3. IMF-based Devices 12
4. Discussion 14
5. References 14
Chapter 3: Characterization of IMF Interfaces Using XRD 16
1. Background 16
2. XRD Models 17
3. Experimental Setup 18
4. Simulations 19
5. XRD Measurements 20
6. XRD Fittings 22
7. Discussion 24
8. Conclusions 25
9. References 25
Chapter 4: GaSb *P-I-N* Photodiodes 26
1. Background 26
2. Acceptor Doping Compensation 28
3. Fabrication 29
4. Room Temperature Characteristics 31
5. Bandwidth Measurements 32
6. *I-V* vs. Temperature Measurements 33
7. *C-V* vs. Temperature Measurements and Admittance Spectroscopy 34
8. Lifetime Measurements 37

9. Repeatability 41
10. Conclusion 42
11. References 42
Chapter 5: Interface Charge Density and Band Offsets 44
1. Background 44
2. Experimental Design 46
3. Fabrication 47
4. *I-V* vs. Temperature Measurements & Activation Energies 48
5. *C-V* vs. Temperature Measurements 49
6. Activation Energies 52
7. Discussion 56
8. Conclusion 56
9. References 57
Chapter 6: Characterization of IMF-based Avalanche Photodiodes 59
1. Background 59
2. Device Design and Fabrication 61
3. $Al_{0.8}Ga_{0.2}As$ Design *I-V* and Responsivity 61
4. $Al_{0.8}Ga_{0.2}As$ Design *C-V* Measurements and *I-V* vs. Temperature 62
5. Further Enhancements using Delta-Doping 63
6. Temperature-Dependent *I-V* of GaAs Design 64
7. Responsivity Measurements of GaAs Design 66
8. Comparison of Responsivity across Designs 68
9. Excess Noise Measurements 69
10. Discussion 70
11. Conclusion 71
12. References 71
Chapter 7: Conclusion 73
1. Five Easy Pieces 73
2. Five Not-So-Easy Pieces 74

Acknowledgments

I would like to thank my adviser, Prof. Diana L. Huffaker, for her never ending support, guidance, and leadership. I would like to thank Prof. Mark S. Goorsky for his guidance, support, and willingness to take a chance. I would like to thank Prof. Dwight C. Streit and Prof. Robert N. Candler for their guidance and support, as well as the ever-present support of their research groups.

I would like to thank Kalyan Nunna and Jun He for taking time to teach me the basics of MBE, even when nothing was going right. I would like to thank Ramesh Laghumavarapu, Jun Tatebayashi, Anitha Jallipalli, and Ping-Show Wong for teaching me the basics of fabrication and characterization. I would like to thank Jin Wang for being the best undergraduate researcher imaginable, as well as Michael J. Jackson and Jeff McKay for helping him (and me) along the way. I would like to thank Andrew J. R. Marshall and Adam P. Craig for setting the golden standard for collaboration. I would like to thank Deeona Columbia, Mandy Smith, and Gershwin Mason for always being there to help. I would like to thank the ASEE SMART Fellowship for funding me and providing me a future at AFRL. I would like to thank Robert Bedford for being a sounding board on the IMF and helping me find a place at AFRL. And finally I would like to thank Baolai Liang and Paul J. Simmonds for their constant guidance, support, enthusiasm, and professionalism.

To the short-timers in the lab – Andrew, Pradeep, Josh, Giacomo, and Adam – I wish you the best and look forward to seeing you in the near future. Our last five years or so have been a wild ride. To those whose first experiments are just beginning – Michael, Meng, Alan, and Bor-Chau – you have it in you to bring the lab to higher heights. Stand on our shoulders and keep climbing.

To my family, for whom I have always tried to keep “a good heads up.”

Vita

August 2001 – June 2005	B.S. Electrical Engineering; B.S. Economics Johns Hopkins University Baltimore, MD, USA
July 2005 – June 2008	Systems Engineer Lockheed Martin Missiles and Fire Control Orlando, FL, USA
January 2006 – June 2008	M.S. Optics University of Central Florida Orlando, FL, USA
June 2008 – June 2013	Graduate Student Researcher University of California, Los Angeles Los Angeles, CA, USA

Publications

1. A. Mahalanobis, C. Reyner, H. Patel, T. Haberfelde, David Brady, Mark Neifeld, B. V. K. Vijaya Kumar, and Stanley Rogers, Proc. of SPIE 6714, 67140D (2007).
2. Liang Baolai, Lin Andrew, Pavarelli Nicola, Reyner Charles, Tatebayashi Jun, Nunna Kalyan, He Jun, J. Ochalski Tomasz, Huyet Guillaume, and L. Huffaker Diana, Nanotechnology 20 (45), 455604 (2009).
3. J. He, C. J. Reyner, B. L. Liang, K. Nunna, D. L. Huffaker, N. Pavarelli, K. Gradkowski, T. J. Ochalski, G. Huyet, V. G. Dorogan, Yu I. Mazur, and G. J. Salamo, Nano Letters 10 (8), 3052 (2010).
4. Charles J. Reyner, Jin Wang, Kalyan Nunna, Andrew Lin, Baolai Liang, Mark S. Goorsky, and D. L. Huffaker, Applied Physics Letters 99 (23), 231906 (2011).
5. Andrew R. J. Marshall, Kalyan Nunna, Siew Li Tan, Charles J. Reyner, Baolai Liang, Anitha Jallipalli, John P. R. David, and D. L. Huffaker, Proc. of SPIE 8541, 85410F (2012).
6. Yu I. Mazur, V. G. Dorogan, G. J. Salamo, G. G. Tarasov, B. L. Liang, C. J. Reyner, K. Nunna, and D. L. Huffaker, Applied Physics Letters 100 (3), 033102 (2012).
7. K. C. Nunna, Tan Siew Li, C. J. Reyner, A. R. J. Marshall, Liang Baolai, A. Jallipalli, J. P. R. David, and D. L. Huffaker, Photonics Technology Letters, IEEE 24 (3), 218 (2012).
8. Paul J. Simmonds, Ramesh Babu Laghumavarapu, Meng Sun, Andrew Lin, Charles J. Reyner, Baolai Liang, and Diana L. Huffaker, Applied Physics Letters 100 (24), 243108 (2012).
9. Jiang Wu, Y. F. M. Makableh, R. Vasan, M. O. Manasreh, B. Liang, C. J. Reyner, and D. L. Huffaker, Applied Physics Letters 100 (5), 051907 (2012).
10. T. Nowozin, L. Bonato, A. Hogner, A. Wiengarten, D. Bimberg, Wei-Hsun Lin, Shih-Yen Lin, C. J. Reyner, Baolai L. Liang, and D. L. Huffaker, Applied Physics Letters 102 (5), 052115 (2013).
11. Meng Sun, Paul J. Simmonds, Ramesh Babu Laghumavarapu, Andrew Lin, Charles J. Reyner, Hsin-Sheng Duan, Baolai Liang, and Diana L. Huffaker, Applied Physics Letters 102 (2), 023107 (2013).
12. Jiri Thoma, Baolai Liang, Charles Reyner, Tomasz Ochalski, David Williams, Stephen P. Hegarty, Diana Huffaker, and Guillaume Huyet, Applied Physics Letters 102 (1), 013120 (2013).

Chapter 1: Introduction

Infrared detector development has been driven by epitaxial growth techniques. While first generation detectors were created using crystal pulling, second and third generation detectors have moved to vapor phase epitaxy and molecular beam epitaxy. These deposition technologies have changed the minimum feature size from millimeters, to micrometers, to nanometers. In turn, device designers have been able to utilize new physical phenomena to maximize the spectral response, quantum efficiency, bandwidth, and detectivity of an infrared detector. Heavily researched applications include thermal imaging, fiber optic communications, and quantum cryptography.

The key limitation to these deposition technologies has been managing strain in the semiconductor crystal. Semiconductors with one lattice constant cannot support high quality epilayers of another. As such, compound semiconductor materials are typically grouped by lattice constant: the 5.65 Å GaAs/AlGaAs "Arsenides", the 5.87 Å InP/InAlAs/InGaAs "Phosphides", and the 6.1 Å GaSb/AlSb/InAs "Antimonides". While researchers have attempted to utilize each group for infrared detectors, the Antimonides are the most promising. The largest range of bandgaps, band alignments, and device designs are possible in this material system. Unfortunately, these are also the most difficult to fabricate and suffer from the least mature substrate technologies. They also do not offer a large bandgap, low noise gain material, unlike AlGaAs in the Arsenides and InAlAs in the Phosphides.

A potential solution to the substrate and gain limitation is the integration of the Antimonides and the Arsenides. The Arsenides are particularly favorable because of the small conduction band discontinuity between GaAs and GaSb; the availability of large diameter (>75 mm), semi-insulating substrates; and counter-intuitively, a large lattice mismatch of 7.8%. The larger mismatch is important, as it determines whether the lattice strain will create 60° threading dislocations or 90° Lomer dislocations. If the lattice strain can be accommodated utilizing Lomer dislocations, it is possible to create an interfacial misfit array (IMF). Such a network of Lomer dislocations effectively relaxes the epilayer at the interface, does not seed any threading dislocations (ideally), and leaves a high quality epilayer for device fabrication. While other options for heterogeneous integration exist – including wafer bonding, metamorphic buffers, and selective area growth – the IMF is unique in that it requires epitaxial control of a single layer of atoms. In this dissertation, the structural, electrical, and optical characterization of IMF-based infrared photodiodes will be examined.

This dissertation begins with a literature review, including an overview of molecular beam epitaxy (MBE). The various lattice-mismatched integration schemes are all listed, highlighting device integration and photodiode performance across wafer bonding, metamorphic buffers, selective area growth, and IMF growth. Results for GaSb/GaAs IMF lasers, photovoltaics, and detectors are also given as a basis for comparison. Several studies have already reported differences between IMF-based and homoepitaxial growth. Common findings across these studies will be emphasized.

The third chapter examines the structural properties of IMF material utilizing x-ray diffraction (XRD). Cross-sectional transmission electron microscopy (TEM) is used to verify the dislocation spacing in the IMF. The dislocation spacing, and corresponding knowledge of the Burgers vector, is then used in conjunction with a theoretical model of XRD broadening to determine the correlation factor of the IMF, or more simply, the degree of perfection across a large area array. The IMF is found to be approximately 99% complete, or one Lomer dislocation per hundred is improperly placed. Thicker GaSb buffers are shown to have thinner FWHM values, even though the dislocation density has not changed. Further evidence is given that the GaSb buffer is over 99.5% relaxed, indicating that threading dislocation generation outside the interface is unlikely. This technique represents a non-destructive measure to verify IMF formation prior to device fabrication.

The fourth chapter focuses on the high bandwidth properties of a GaSb homojunction based on an *n*-GaAs/*n*-GaSb IMF. The key features of this device are the semi-insulating GaAs substrate, an ohmic *n*-GaAs contact and the introduction of Tellurium compensation doping in the intrinsic region.

Collectively, these improvements increase the frequency response of the photodiode, improve its responsivity, and limit its leakage. Additional studies of carrier lifetime and defect levels in the material are also given to validate material quality relative to bulk growth. These results represent the current world record bandwidth for GaSb homojunction photodiodes.

The fifth chapter concentrates on the interface charge density at the *p*-GaSb/*p*-GaAs heterointerface. The IMF is shown to behave as a sheet of acceptors, as expected. However, the acceptor sheet density is found to be 1.81×10^{12} cm^{-2}, or only 60% of the dangling bond density (3.1×10^{12} cm^{-2}). These densities are 1-2 orders of magnitude greater than interface charge densities found in lattice-matched semiconductors, e.g. AlGaAs/GaAs, InGaP/GaAs, etc. Silicon delta-doping is added near the interface in order to compensate such a high interface charge density. The band offset, depletion through the interface, and diode leakage current are shown to be controllable.

And finally, the sixth chapter of this dissertation builds upon the bandwidth and interface charge studies to create an IMF-based avalanche photodiode (APD). In this structure, the absorber is *p*-GaSb and the multiplication region is either GaAs or AlGaAs. The structures show how it is possible to utilize the IMF charge sheet to stop depletion in the multiplication region, leading to higher electric fields and gain. As such, the IMF is useful not only from a crystal growth perspective, but from a device perspective. The different multiplication regions also exemplify the trade-off between excess noise and carrier collection efficiency, with lower excess noise in the AlGaAs multiplication region and higher carrier collection efficiency in the GaAs multiplication region. Further studies of delta-doping in the GaAs multiplication region show how the barrier between the GaAs and GaSb can be lowered without affecting the fields.

Chapter 2: Literature Review

1. Overview of Molecular Beam Epitaxy

Molecular beam epitaxy (MBE) was invented by J. R. Arthur and A. Y. Cho at Bell Laboratories between 1968 and 1973.[1] It differentiates itself from other deposition techniques because of its slow deposition rates, its ultra-high vacuum (UHV) background (10^{-11} to 10^{-9} Torr), and its non-equilibrium conditions (there are typically 10x more arsenic atoms incident on the substrate than gallium atoms, yet a stoichiometric crystal forms). Solid-source MBE is the sole technique used in this dissertation, where the constituent materials (Al, Ga, In, As, Sb, Te, Be, and Si) are all placed inside the vacuum chamber in highly-purified form (>99.99999% purity). The source materials are then heated in pyrolytic boron nitride (PBN) crucibles to temperatures at which a sizeable flux of atoms will be either boiled or sublimated away (vapor pressures between 10^{-4} to 10^{-2} Torr). To commence growth, a substrate is placed in front of the sources and heated. The substrate temperature is generally limited by two factors. It must be high enough to promote atom migration on the surface, and it must be low enough to avoid excess desorption of the Group III atoms. The heated source crucibles feature pneumatic shutters to enable on/off control of the deposition. Control of the deposition rate, or the composition in the case of a ternary or quaternary compound, is achieved by controlling the source temperatures.

MBE is unique because of the characterization tools available. Infrared pyrometry is routinely used to monitor the substrate temperature, and can be calibrated for various substrate materials and mounting configurations. A residual gas analyzer (RGA) is typically also mounted to the vacuum chamber. The RGA allows quantitative assessments of the gas species in the reactor during growth, including deep level trap centers such as Oxygen. The RGA is especially important during maintenance, as it can be tuned to Helium's mass and used as a leak detector. Finally, reflection high-energy electron diffraction (RHEED) is perhaps the single-most important characterization technique in MBE. The UHV environment provides a mean free path much larger than the reactor size for electrons emitted from a filament. These electrons graze the substrate at angles between 2-3°, where they diffract off of the surface reconstruction of Group V atoms. The diffraction pattern is captured using a phosphor screen. The RHEED pattern can be used to measure deposition rates, calibrate substrate temperatures, determine quantum dot formation, and monitor crystal quality. Since the mean free path of the electron in the crystal is several angstroms, the diffraction pattern samples only the top layer of atoms.

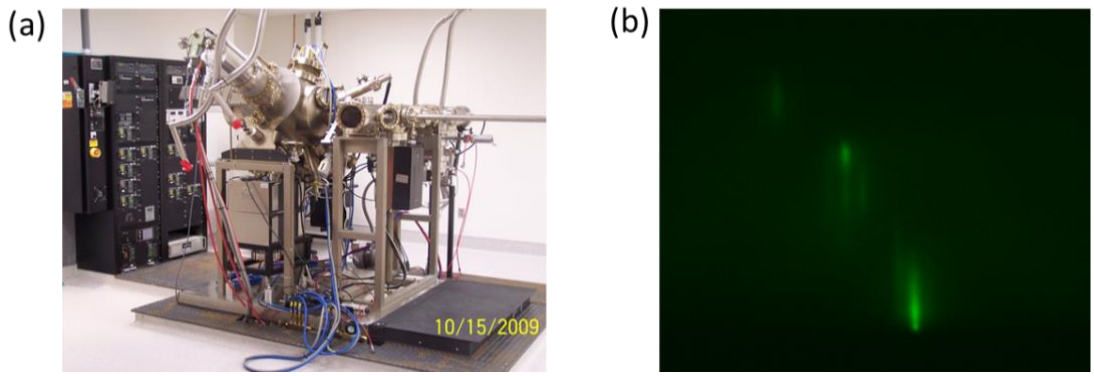

Figure 1: Image of As/Sb MBE at UCLA CNSI. (b) RHEED image of GaAs surface reconstruction

2. Lattice-Mismatched Semiconductors

Integration of lattice-mismatched semiconductors has and continues to be a topic of ongoing research in both MBE and its principal alternative, metal-organic vapor phase epitaxy (MOVPE). This research goal typically takes two different approaches: one which seeks to use lattice-mismatch to create new semiconductor structures, e.g. quantum dots; and one which acknowledges the lattice mismatch, but seeks to avoid its consequences, e.g. metamorphic buffers. The central problem is effectively one of strain. As lattice-mismatched material is deposited, the strain energy in the crystal increases, leading to increased surface roughness or dislocation formation.[2] The thickness at which the dislocations start to form is called the critical thickness. Matthews and Blakeslee were the first to define a generalized formula for critical thickness based on a GaAs and $GaAs_{0.5}P_{0.5}$ superlattice.[3] Further refinements of the general formula incorporated the kinetics of dislocation formation, i.e. dislocation glide and dislocation nucleation.[4] However, the dislocation mechanisms by Matthews and others were all for thin films. Other limitations include the role of surface energetics, or the 2D-3D transition, which are utilized for quantum dot formation. At this thickness, it is energetically favorable for a thin film to form islands as opposed to dislocations. Island coalescence can determine dislocation nucleation, and calculations are heavily dependent on the surface energies of the epilayer.[5]

There are many approaches to integrating lattice-mismatched thin films onto a substrate, especially materials such as GaAs and GaSb with a large lattice-mismatch (7.8%). However, four general categories can be identified. The categories are metamorphic buffers, wafer bonding, selective area growth, and interfacial misfit arrays (the focus of this dissertation). These four general categories can be further limited into the number of researchers who have attempted to grow Antimonides. Each category has specific advantages and disadvantages, mostly related to the amount of processing required before growth, the growth conditions, and the amount of processing required after growth. For instance, selective area growth and wafer bonding both require significant processing time before and after growth, respectively. Meanwhile, the major advantage of the IMF technique relative to metamorphic buffers is the deposition time. It is not uncommon to find metamorphic buffers larger than 5 µm thick, which requires multiple hours of deposition time using high-quality growth techniques, or shorter, lower-quality growth.[6]

2.1. Selective Area Epitaxy

Selective area epitaxy (SAE) growth of Antimonides has been defined by both 2D and 3D growth modes. These techniques have focused on using metalorganic vapor phase epitaxy (MOVPE) with thin dielectric masks (typically SiO_2 or SiN_x) to increase the critical thickness. The results have mostly favored the creation of 2D films, as opposed to 3D nanopillar structures. For instance, Jha et al. used block co-polymers (polystyrene in polymethylmethacrylate) to pattern GaAs (100) substrates with 20 nm holes at 40 nm pitch.[7] They were able to show a significant reduction in the FWHM of the GaSb 004 x-ray diffraction (XRD) peak using a nano-patterned substrate, as opposed to an unpatterned surface (see Figure 2 (a). Unfortunately, the nanopatterned material exhibited an abundance of twinning (switching between the zincblende and wurtzite crystal structures). These results were also compared to $In_xGa_{1-x}As$ growth using the same technique, and high Indium concentrations were shown to favor non-planar growth modes.[8]

(a)

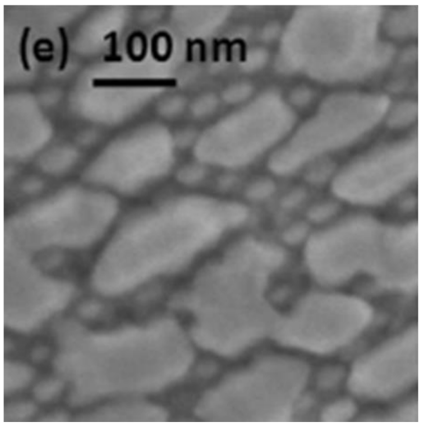

(b)

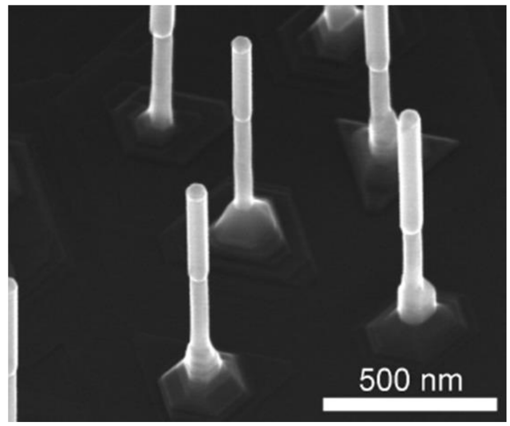

Figure 2: (a) GaSb thin film growth using block polymers from Jha.[7] (b) InGaAs/GaSb tunnel diodes from Borg.[9]

SAE growth of GaSb nanopillars on GaAs (111)B surfaces has also been reported by multiple groups.[10,11] These structures are intriguing, in that the lattice-mismatch does not create misfit dislocations as it would in planar integration schemes, but instead leads to lateral expansion of the pillar.[11,12] There are no reports of devices using a GaSb nanopillar on GaAs, however researchers have demonstrated InGaAs/GaSb band-to-band tunneling on an InAs substrate (see Figure 2 (b)).[9] A central problem facing researchers in this field are the low melting points of GaSb at 712°C, which is exacerbated by antimony's low sticking coefficient above 600°C, and the high cracking temperature of common antimony precursors in MOVPE (>450°C).

2.2. Wafer Bonding

Wafer bonding of GaSb has mostly focused on placing the Antimonide active region onto a semi-insulating substrate. Several groups have attempted to bond GaSb to GaAs. Zheng et al. first attempted to bond GaSb with GaAs using a borosilicate glass (BSG) layer.[13] The first step was the implantation of hydrogen below the wafer surface. Next, the wafer was bonded to the BSG layer at 100°C, and subsequently heated to 160°C to split the GaSb. The transferred layer featured a XRD FWHM of 147" on the GaSb 004 peak, which was considered good relative to direct growth of GaSb on GaAs. Serious issues of blistering remained. Wang et al. directly bonded two substrates (GaSb and GaAs) in a step forward for electronic integration (see Figure 3 (a)).[14] The substrates were bonded at temperatures of 350-480°C, both with and without pressure. Utilizing photoluminescence and XRD, Wang was able to demonstrate that a grooved substrate bonded without pressure prevented damage to the active region.

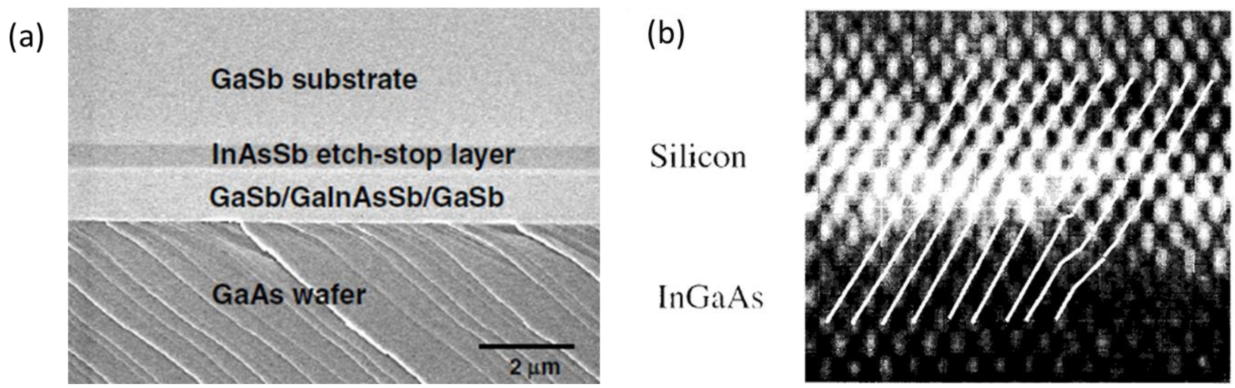

Figure 3: (a) Scanning electron microscope image of GaSb heterostructure fused to GaAs using pressure at 400°C from Wang. (b) Cross-sectional TEM of interface between InGaAs and Si from Hawkins.[15]

Wafer bonding of other materials has led to high performance devices. Hawkins et al. demonstrated an InGaAs avalanche photodiode on silicon using wafer bonding (see Figure 3 (b)).[15] The bonding required mating the silicon substrate and InGaAs material at 650°C in a H_2 ambient under pressure. Gain bandwidth products of 81 GHz were achieved, at gains of over 100. However, the unity gain bandwidth was below 1 GHz, and appeared to be a direct result of the series resistance at the interface. Further improvements lead to unity gain bandwidths beyond 13 GHz.[16] Moran et al. focused on the lack of semi-insulating GaSb substrates, and bonded an Antimonide heterojunction bipolar transistor to a sapphire (Al_2O_3) substrate.[17] The bonded active region experienced XRD broadening as it was transferred to the sapphire substrate from the growth substrate, and a factor of 2 decrease in DC gain.

2.3. Metamorphic Buffers

The purpose of every metamorphic buffer is to provide a defect-free surface at a specific lattice constant by trading off substrate cost and growth time. Metamorphic buffers typically achieve this goal by compositionally grading the epilayer, or by changing the periodicity of a superlattice. Mendach et al. demonstrated that it was possible to grade the lattice-constant from GaAs (5.65 Å) to 5.96 Å using an $In_xAl_{1-x}As$ metamorphic buffer.[18] As seen in Figure 4 (b), dense dislocation networks could be found in the graded approach, but these were mostly localized inside the lower portions of the metamorphic buffer. Yang et al. attempted to create a 5.87 Å top surface using both GaAsSb and InGaAsP alloys.[19] The resultant buffers exhibited threading dislocation densities of $< 10^6$ cm^{-2} at the surface, which approached substrate quality. However, these buffers were grown using miscut substrates and MOVPE, which somewhat limits their future use. A major limitation of metamorphic buffer technologies is that it becomes increasingly difficult to utilize the metamorphic buffer as any more than a structural component if the dislocation density is too high inside any part of the buffer layer, as the dislocations serve as recombination centers for minority carriers and affect the series resistance of the device.

Devices based on metamorphic buffers have shown considerable promise. Jang et al. have demonstrated that it is possible to fabricate extremely high bandwidth InGaAs photodiodes on GaAs substrates using metamorphic buffers (see Figure 4 (b)).[20] Frequency cut-offs near 50 GHz, with responsivity values of 0.43 A/W at 1.55 μm and single nanoamp dark current values were produced. However, these results only bridged the 3.8% lattice mismatch between GaAs and $In_{0.53}Ga_{0.47}As$, where InP substrates are readily available. A more interesting approach has been pursued by Geisz et al., who created a triple-junction solar cell that passed photocurrent through an $In_xGa_{1-x}P$ metamorphic buffer.[21] Key advancements included the use of multi-beam optical stress sensors to verify film stress during growth, and the use of a compressively strained metamorphic buffer with a tensile strained InGaAs epilayer. The layers were designed to leave a stress-free wafer at the end of the growth, which prevented the nucleation of any dislocations. However, the overall lattice-mismatch of the system was only 2.1%.

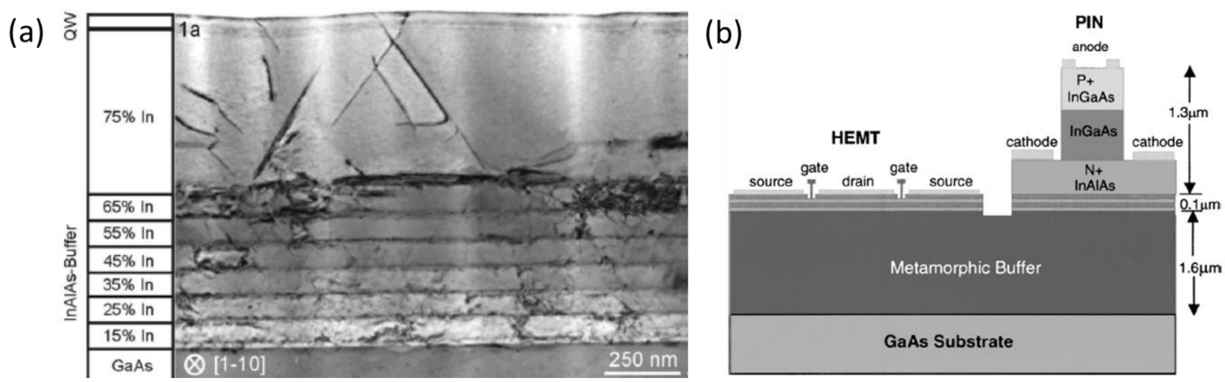

Figure 4: (a) Cross-sectional TEM of metamorphic buffer from Mendach.[18] (b) Integration of PIN and HEMT structure on a metamorphic buffer for high bandwidth performance from Hoke.[22]

2.4. Interfacial Misfit Arrays

Misfit arrays have been known to exist for some time,[4] however the first experimental results for GaSb on GaAs were by Qian et al in 1997.[23] Qian used atomic force microscopy (AFM) to show the formation of islands after several nanometers of GaSb growth. These islands were elongated in the $[1\bar{1}0]$ direction, and featured (111) sidewalls. As the deposition increased, the islands expanded and nucleated further 90° dislocations at the sidewall. The density of threading dislocations (60° dislocations) was found to be completely independent of growth time. Qian interpreted the constant threading dislocation density as evidence that island coalescence was not the source of threading dislocations, but that these unwanted dislocations were initiated by the GaSb deposition (see Figure 5 (a)). No effort was made to optimize the deposition conditions. Huang et al. were the first to fully optimize the growth conditions of the misfit array (now called an IMF) by removing the excess arsenic from the surface.[24] Huang was able to reduce the etch pit density to less than 10^6 cm^{-2}, as compared to reported values of 10^3 from substrate manufacturers. There is some discrepancy in IMF growth techniques across the literature. While recent authors all agree that the elimination of arsenic from the surface is the primary concern, the choice to switch from antimony to arsenic is done at both the GaAs deposition temperature and the GaSb deposition temperature.[25]

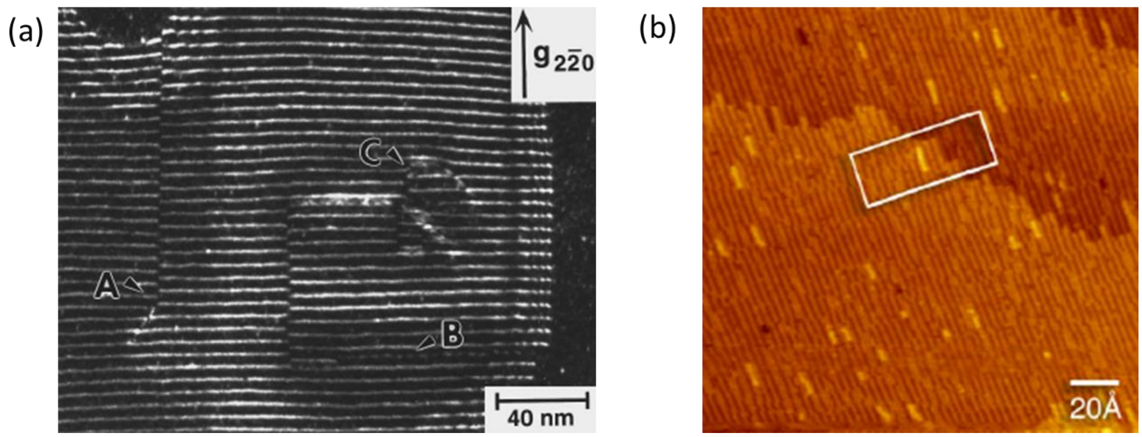

Figure 5: (a) Weak beam TEM of 20 nm of GaSb on GaAs showing dislocation alignment from Qian.[23] (b) Scanning tunneling microscopy of (2x8) reconstruction after soaking GaAs surface with Sb_2 from Bickel.[26]

The fundamental difference between IMF and other lattice-mismatched integration schemes is the precise control of a single monolayer of atoms, and the switching sequence is of critical importance. The IMF requires not only the removal of the arsenic surface to expose gallium, but also the correct arrangement of the antimony. Key differences exist between various research groups. Richardson et. al cool from 580°C to 505°C under As_2 overpressure. The arsenic valve and shutter are then closed, which is verified by a change from a c(4x4) reconstruction to a (2x4) reconstruction in the RHEED. The Sb_2 and gallium molecular beams then commence simultaneously to begin growth. Wang et al. have a different approach.[27,28] Wang grew GaAs at 580°C, but then removed both gallium and As_2 molecular beams in order to cool to 460-485°C. At that substrate temperature, Sb_2 overpressure was applied, leading to a surface reconstruction shift to (1x3) and (2x8) (see Figure 5 (b)). All growths discussed in this manuscript feature a sequence based on Huang et al.[24] After GaAs growth at 580°C, the arsenic valve is closed, followed by the shutter. During this time, the surface reconstruction switches from a (2x4) to a (1x1) reconstruction. After a short pause, the antimony shutter is opened and the (1x1) reconstruction switches to a (2x8) reconstruction. The substrate is then cooled to 510°C under Sb_2 overpressure. The addition of gallium leads to a 3D RHEED pattern, indicating island formation. This pattern quickly dissipates and leaves the normal (1x3) GaSb reconstruction. A schematic of a fully formed IMF, with a clean switch from As to Sb, is shown in Figure 6.

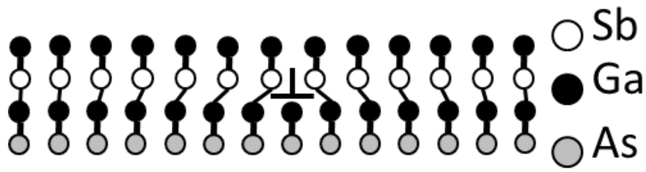

Figure 6: Schematic of IMF. The upside down T is a Lomer dislocation.

3. IMF-based Devices

State of the art IMF-based devices can be found in multiple device fields, including lasers, detectors, and transistors. No common themes exist across the device fields, as both economic and engineering arguments are used to justify the introduction of GaAs substrates. The first reports of IMF-based devices focused mostly on lasers. IMF-based lasers have two key advantages over designs using GaSb substrates, assuming a vertical cavity orientation. The principle advantage is the use of commercially-available Distributed Bragg Reflector (DBR) substrates. These substrates utilize an AlGaAs/GaAs DBR grown via MOVPE and integrate an Antimonide active region using the IMF growth mode in MBE. The second advantage is that the thermal conductivity of GaAs is approximately five times greater than GaSb.[29] The use of a GaAs substrate should therefore decrease the temperature dependence of the optical output power and lasing threshold. Other advantages related to design and fabrication – the use of selective etches, oxide apertures, coupled GaAs/GaSb active regions, etc. – have yet to be realized or explored.

Multiple groups have attempted to produce lasers on IMF templates.[30-35] While none of these devices have reached the same level of performance as devices grown on GaSb substrates, direct comparisons have been made. Laurain et al. showed that the higher threshold power required for lasing in an IMF-based device could be directly attributed to nonradiative losses caused by Shockley-Read-Hall (SRH) recombination.[35] These losses remove carriers that could otherwise be used for gain from the active region. The calculated SRH lifetime of the IMF-based device was 2.6 ns, as compared to 16 ns in a device grown on a GaSb substrate.

The second focus of IMF-based devices has been photodiodes. Nunna et al. showed that InGaAsSb absorbers on IMF-based templates had similar detectivities to their homoepitaxial counterparts.[36] This finding was further enhanced by Marshall et al., who demonstrated that the limiting factor in the detector performance was not the bulk region, but surface recombination from the etch schemes.[37] Plis et al. also demonstrated that IMF-based designs were not a limiting factor in InAs/GaSb strained layer superlattices.[38] The detectivity of both homoepitaxial and IMF-based diodes were 10^9 Jones at room temperature. Alternative *p-i-n* designs (as opposed to nBn) behaved similarly, which was surprising. The nBn architecture is less dependent on minority carrier lifetime than the corresponding photodiode design.[39] Similar trends in both indicated that the IMF was not limiting these devices.

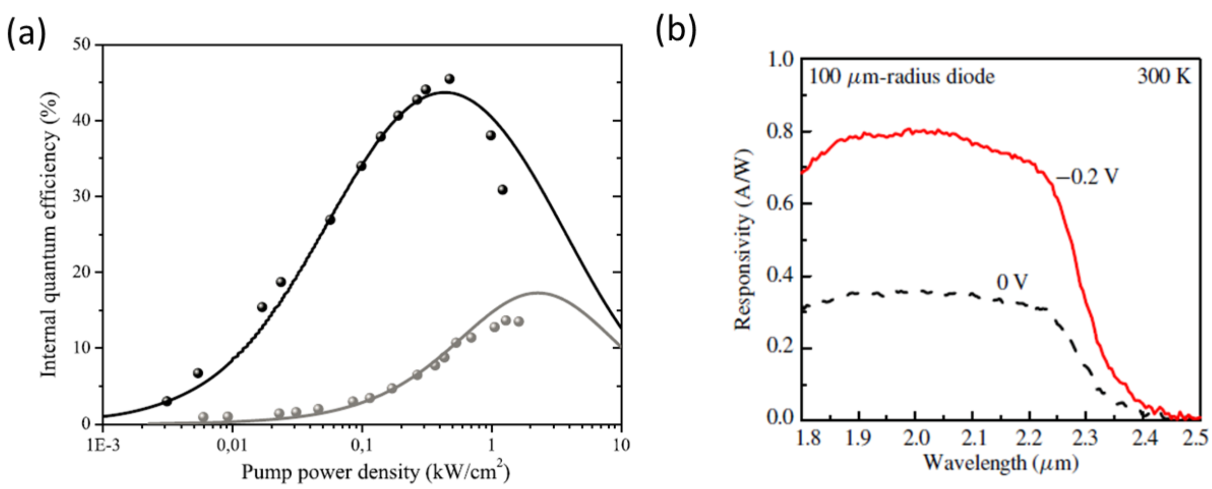

Figure 7: (a) Internal quantum efficiency of homoepitaxial (black dots) and IMF-based (grey dots) lasers from Laurain.[35] (b) Responsivity of IMF-based InGaAsSb photodiodes with similar performance to homoepitaxial photodiodes from Nunna.[36]

4. Discussion

There are several integration techniques available to device designers for integration of Antimonides on Arsenides. While some of these integration schemes are still in their infancy, i.e. selective area epitaxy, more robust results can be found with wafer bonding, metamorphic buffers, and IMF. Metamorphic buffers have shown a high degree of performance, and have produced many devices, but typically have not bridged the entire 7.8% lattice mismatch between GaAs and GaSb. The IMF growth technique is by far the leader in number of minority carrier devices produced for the Antimonides, and has exhibited similar performance to homoepitaxial growth in several reports. It is therefore the best approach for minority carrier devices such as photodiodes.

5. References

[1] W. Patrick McCray, Nat Nano **2** (5), 259 (2007).

[2] J. Tersoff and F. K. LeGoues, Physical Review Letters **72** (22), 3570 (1994).

[3] J. W. Matthews and A. E. Blakeslee, Journal of Crystal Growth **27** (0), 118 (1974).

[4] E. A. Fitzgerald, Materials Science Reports **7** (3), 87 (1991).

[5] Holger Eisele and Mario Dähne, Journal of Crystal Growth **338** (1), 103 (2012).

[6] V. K. Yang, M. Groenert, C. W. Leitz, A. J. Pitera, M. T. Currie, and E. A. Fitzgerald, Journal of Applied Physics **93** (7), 3859 (2003).

[7] Smita Jha, C. C. Liu, T. S. Kuan, S. E. Babcock, P. F. Nealey, J. H. Park, L. J. Mawst, and T. F. Kuech, Applied Physics Letters **95** (6), 062104 (2009).

[8] Smita Jha, Monika K. Wiedmann, T. S. Kuan, Xueyan Song, S. E. Babcock, and T. F. Kuech, Journal of Crystal Growth **315** (1), 91 (2011).

[9] B. Mattias Borg, Kimberly A. Dick, Bahram Ganjipour, Mats-Erik Pistol, Lars-Erik Wernersson, and Claes Thelander, Nano Letters **10** (10), 4080 (2010).

[10] Y. N. Guo, J. Zou, M. Paladugu, H. Wang, Q. Gao, H. H. Tan, and C. Jagadish, Applied Physics Letters **89** (23), 231917 (2006).

[11] Mattias Jeppsson, Kimberly A. Dick, Jakob B. Wagner, Philippe Caroff, Knut Deppert, Lars Samuelson, and Lars-Erik Wernersson, Journal of Crystal Growth **310** (18), 4115 (2008).

[12] Frank Glas, Physical Review B **74** (12), 121302 (2006).

[13] Y. Zheng, P. D. Moran, Z. F. Guan, S. S. Lau, D. M. Hansen, T. F. Kuech, T. E. Haynes, T. Hoechbauer, and M. Nastasi, Journal of Electronic Materials **29** (7), 916 (2000).

[14] C.A. and Liau Wang, Z.L. and Shiau,D.A. and Nitishin,P.M., MRS Proceedings **768** (G4.3) (2003).

[15] Aaron R. Hawkins, Thomas E. Reynolds, Derek R. England, Dubravko I. Babic, Mark J. Mondry, Klaus Streubel, and John E. Bowers, Applied Physics Letters **68** (26), 3692 (1996).

[16] B. F. Levine, A. R. Hawkins, S. Hiu, B. J. Tseng, J. P. Reilley, C. A. King, L. A. Gruezke, R. W. Johnson, D. R. Zolnowski, and J. E. Bowers, Applied Physics Letters **71** (11), 1507 (1997).

[17] P. D. Moran, D. Chow, A. Hunter, and T. F. Kuech, Applied Physics Letters **78** (15), 2232 (2001).

[18] S. Mendach, C. M. Hu, Ch Heyn, S. Schnüll, H. P. Oepen, R. Anton, and W. Hansen, Physica E: Low-dimensional Systems and Nanostructures **13** (2–4), 1204 (2002).

[19] Li Yang, Mayank T. Bulsara, Kenneth E. Lee, and Eugene A. Fitzgerald, Journal of Crystal Growth **324** (1), 103 (2011).

[20] J. H. Jang, G. Cueva, R. Sankaralingam, P. Fay, W. E. Hoke, and I. Adesida, Photonics Technology Letters, IEEE **15** (2), 281 (2003).

[21] J. F. Geisz, Sarah Kurtz, M. W. Wanlass, J. S. Ward, A. Duda, D. J. Friedman, J. M. Olson, W. E. McMahon, T. E. Moriarty, and J. T. Kiehl, Applied Physics Letters **91** (2), 023502 (2007).

[22] W. E. Hoke, R. E. Leoni, C. S. Whelan, T. D. Kennedy, A. Torabi, P. F. Marsh, Y. Zhang, C. Xu, and K. C. Hsieh, Journal of Vacuum Science & Technology B: Microelectronics and Nanometer Structures **22** (3), 1554 (2004).

[23] W. Qian, M. Skowronski, R. Kaspi, M. De Graef, and V. P. Dravid, Journal of Applied Physics **81** (11), 7268 (1997).

[24] S. H. Huang, G. Balakrishnan, A. Khoshakhlagh, A. Jallipalli, L. R. Dawson, and D. L. Huffaker, Applied Physics Letters **88** (13), 131911 (2006).

[25] C. J. K. Richardson, L. He, and S. Kanakaraju, Journal of Vacuum Science & Technology B: Microelectronics and Nanometer Structures **29**, 03C126 (2011).

[26] Jessica E. Bickel, Normand A. Modine, and Joanna Mirecki Millunchick, Surface Science **603** (19), 2945 (2009).

[27] Yi Wang, P. Ruterana, S. Kret, J. Chen, S. El Kazzi, L. Desplanque, and X. Wallart, Applied Physics Letters **100** (26), 262110 (2012).

[28] Yi Wang, P. Ruterana, S. Kret, S. El Kazzi, L. Desplanque, and X. Wallart, Applied Physics Letters **102** (5), 052102 (2013).

[29] M. G. Holland, Physical Review **134** (2A), A471 (1964).

[30] J. B. Rodriguez, L. Cerutti, and E. Tournié, Applied Physics Letters **94** (2), 023506 (2009).

[31] J. Tatebayashi, A. Jallipalli, M. N. Kutty, S. H. Huang, G. Balakrishnan, L. R. Dawson, and D. L. Huffaker, Applied Physics Letters **91** (14), 141102 (2007).

[32] M. Mehta, A. Jallipalli, J. Tatebayashi, M. N. Kutty, A. Albrecht, G. Balakrishnan, L. R. Dawson, and D. L. Huffaker, Photonics Technology Letters, IEEE **19** (20), 1628 (2007).

[33] Thomas J. Rotter, Jun Tatebayashi, Pradeep Senanayake, Ganesh Balakrishnan, Marcel Rattunde, Joachim Wagner, Jorg Hader, Jerome V. Moloney, Stephan W. Koch, L. Ralph Dawson, and Diana L. Huffaker, Applied Physics Express **2** (Copyright (c) 2009 The Japan Society of Applied Physics), 112102 (2009).

[34] Lai Yi-Ying, J. M. Yarborough, Y. Kaneda, J. Hader, J. V. Moloney, T. J. Rotter, G. Balakrishnan, C. Hains, and S. W. Koch, Photonics Technology Letters, IEEE **22** (16), 1253 (2010).

[35] Alexandre Laurain, Jörg Hader, Yi-Ying Lai, Tsuei-Lian Wang, Mike Yarborough, Ganesh Balakrishnan, Thomas J. Rotter, Pankaj Ahirwar, and Jerome V. Moloney, 82420S (2012).

[36] K. C. Nunna, Tan Siew Li, C. J. Reyner, A. R. J. Marshall, Liang Baolai, A. Jallipalli, J. P. R. David, and D. L. Huffaker, Photonics Technology Letters, IEEE **24** (3), 218 (2012).

[37] Andrew R. J. Marshall, Kalyan Nunna, Siew Li Tan, Charles J. Reyner, Baolai Liang, Anitha Jallipalli, John P. R. David, and D. L. Huffaker, Proc. of SPIE **8541**, 85410F (2012).

[38] E. Plis, J. B. Rodriguez, G. Balakrishnan, Y. D. Sharma, H. S. Kim, T. Rotter, and S. Krishna, Semiconductor Science and Technology **25** (8), 085010 (2010).

[39] S. Maimon and G. W. Wicks, Applied Physics Letters **89** (15), 151109 (2006).

Chapter 3: Characterization of IMF Interfaces Using XRD

1. Background

There are several well-established methods to determine the structural quality of a heterointerface. These methods typically provide a trade-off between resolution, sample size, and sample preparation. For instance, cross-sectional transmission electron microscopy (TEM) and cross sectional scanning tunneling microscopy (STM) provide a very high resolution (<10 pm resolution) images of an interface, but are limited in their sample sizes (<1 μm^2). Meanwhile, other methods such as etch pit density (EPD) are capable of extremely large sampling areas (>1 cm^2), but cannot resolve much more than the dislocation type and dislocation density. All three of these techniques are destructive in nature, as the underlying material cannot be reused for device processing or further material studies. A non-destructive technique that provide <100 pm resolution and large sampling areas is necessary.

X-ray diffraction (XRD) is routinely used to characterize the quality of thin films. The primary advantages of XRD are that it is nondestructive, it can quickly sample 1 mm^2 or more at a time, and it can measure far below the surface of the sample (>10 μm). Unfortunately, while it can accurately determine the out-of-plane lattice spacing to within <1 pm, it cannot identify dislocations as easily. However, given the right assumptions, some insights are available.

Previously, IMF characterization techniques have focused on determining threading dislocation density using cross sectional transmission electron microscopy, etch-pit density, or by analyzing island coalescence using surface probe microscopy.[1] None of these techniques allows researchers to characterize the degree of IMF uniformity nondestructively, or over a large area. Other works have used XRD to analyze threading dislocation formation using Williamson-Hall plots, grazing incidence diffraction, or x-ray scattering from the dislocations.[2] These methods typically involve mapping several reciprocal lattice points (RLPs), or require the use of a synchrotron.[2]

2. XRD Models

There are two complementary models of XRD broadening in epitaxial layers with dislocations. The first is called the "mosaic blocks" model.[3] This model interprets random threading dislocations as grain boundaries in the crystal, which give rise to both angular distortion and lattice constant variation. These components are shown in Figure 8.The contribution of each can be quantified based on *a priori* knowledge of the dislocation type, which in turn can be used to calculate the dislocation density. Researchers have been able to accurately model both InGaN/GaN and InGaAs/GaAs structures based on this technique.[4] Unfortunately, there are two implicit assumptions built into this model that make it unsuitable for modeling the IMF. The first is that the dislocations must be randomly distributed. The assumption can be taken for granted in low dislocation density systems, where the forces of each dislocation have little effect on the formation of other dislocations, but not in highly dislocated systems. The second assumption is that the dislocations must have a threading component, which is used to delineate the mosaic blocks and model the scattering. An IMF has a very small proportion of threading dislocations, which makes the contributions of the Lomer dislocations the predominant broadening mechanism.

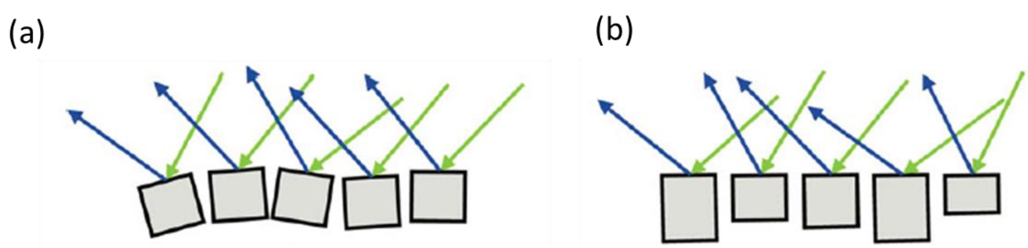

Figure 8: "Mosaic blocks" model of XRD broadening. Broadening is determined by two components: (a) angular distortion and (b) lattice constant variation. Both images from Rago.[5]

A better model for broadening in the IMF is needed, and that that model is perhaps best called the "correlation" model. In this model, the dislocation density is not only localized to a single layer, but the dislocation spacing itself is highly correlated. A model built upon these conditions was first described by Kaganer, et al.[6] Kaganer demonstrated that if the product of the epitaxial layer thickness (d) and the linear dislocation density (ρ) are large enough (ρd>>1), then an analytical expression can be used to describe the peak broadening. Figure 9 shows the theoretical structure, with dislocations all originating at the same distance *d* from the surface. Note that these dislocations can have threading components, as long as the dislocation originates at *d*. Experimental evidence agreeing with this theory has been shown in various material systems, mostly for materials with lattice mismatch >4%.[7] The weakest assumption of this theory is that the layer must be completely relaxed, which holds for GaAs/Si, but is not necessarily true in all cases.[8] However, the "correlation" model is much better suited for IMF characterization than the "mosaic blocks" model.

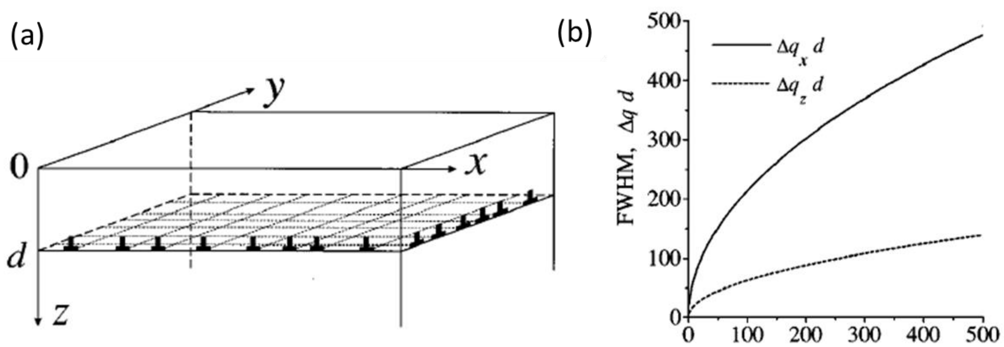

Figure 9: (a) Diagram of "correlated" model of misfit dislocation. Note that the dislocations are all localized at a distance d from the surface. (b) Calculated relationship of FWHM values for 60° dislocations. Both images from Kaganer.[6]

3. Experimental Setup

The correlation model requires several samples and a specific diffractometer set-up. The samples must simply provide several values of ρd to fit against, and ρd must be greater than 1 in all instances. The expected value of ρ is 0.16-0.20 nm^{-1}, hence undoped IMF buffers of 250, 500, 1000, and 1500 nm thicknesses were created. The samples were then placed on a Bede D1 high resolution diffractometer with Maxflux x-ray optics, a beam collimator crystal, and an analyzer crystal. The analyzer crystal is vital for accurate measurements of the x-ray broadening, and previous calibrations on a silicon (100) substrate indicated that the system resolution with the analyzer crystal was between 1-5 arcsec.

Prior to XRD analysis, an IMF buffer was analyzed using TEM to verify the dislocation spacing and measure the material quality. As shown in Figure 10 (a), the IMF formed well and the dislocation spacing was approximately 5.6 nm, or ρ of 0.1786 nm^{-1}. A second analysis was done by taking the Fourier transform of the image to verify the existence of two distinct lattice constants, and not a gradual change. This analysis is found in Figure 10 (b). The Fourier transform shows two distinct intensity peaks at each diffraction condition: the outer point for GaAs and the inner point for GaSb. The points are also in-line with the zero-order diffraction condition, indicating that no lattice tilt has taken place.

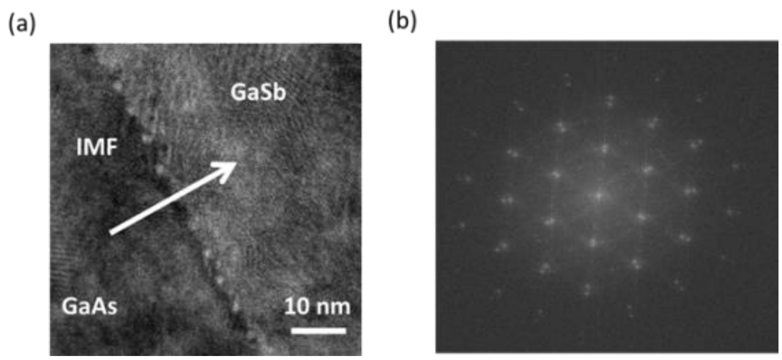

Figure 10: (a) TEM of IMF interface. The array indicates the growth direction. (b) FFT of the TEM shown. Two clear points are visible at each diffraction condition, indicating different lattice constants.

4. Simulations

The correlation model exhibits different trends for each RLP. Kaganer gives only the expected values of the 004 and 224 grazing exit (GE) RLP in his report, so a simulation of the various RLPs was done to provide insight into the shape of the curves. The general formula for the intensity peaks at each RLP is as follows:

$$I(q_x, q_z) = \pi \int_0^d \frac{\partial z}{\sqrt{w_x w_z}} \exp\left[-\frac{\left(q_x - q_{x0}\right)^2}{4w_x} - \frac{\left(q_z - q_{z0}\right)^2}{4w_z} \right]$$

$$w_x\left(0\right) = \frac{\rho Q_z^2 b_x^2}{8\pi d}$$

$$w_z\left(0\right) = \frac{\rho Q_z^2 b_x^2}{8\pi d}\left[\frac{\nu}{1-\nu}\right]$$

Equation 1: Equations governing XRD peak broadening in IMF structures.

These equations hold for all 90° dislocations. The intensity distribution is Gaussian in nature, and a quick analysis of the formula indicates that all FWHM values will be proportional to $Q_z b_x(\gamma\rho d^{-1})^{0.5}$, where γ is the correlation factor, b_x is the Burgers vector of the dislocation, and Q_z is the location in reciprocal space. Since the Burgers vector and the location in reciprocal space remain virtually unchanged (and are generally well defined for III/V materials), this equation can be further simplified to $K(\gamma\rho d^{-1})^{0.5}$, where K is defined for every RLP.

Figure 11 shows the results of these simulations. As expected, only the 004 RLP lies parallel to the $\mathbf{Q_z}$ and $\mathbf{Q_x}$ diffraction vectors, all of the other RLPs are tilted. Furthermore, the simulated RSMs become wider with higher order diffraction conditions, even though the dislocation density remains unchanged. This broadening has been seen on many strained systems, and standard corrections (including Williamson-Hall plots) typically take this into account in order to calculated dislocation densities.[8] Finally, all of the RSMs (except for the 115 RLP) display a low degree of asymmetry.

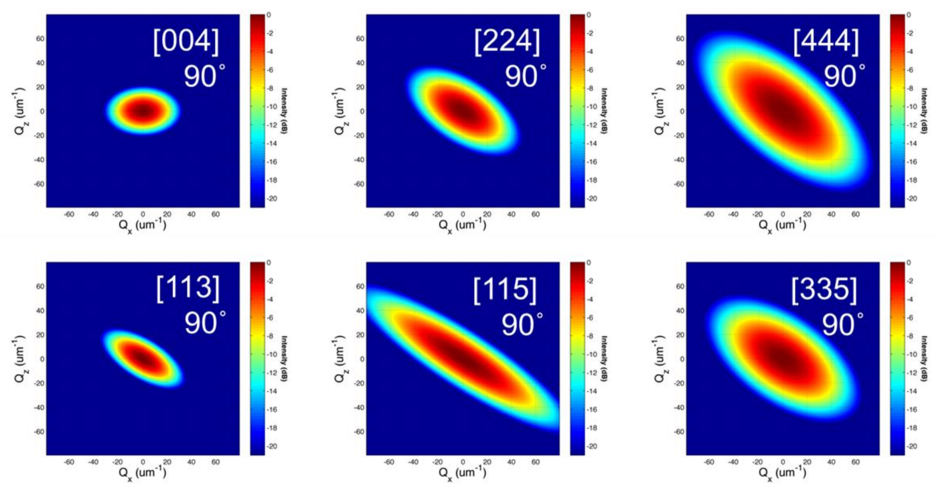

Figure 11: Simulations of RSMs at different reciprocal lattice points and 90° dislocation arrays for a GaSb/GaAs interface with correlation factor of 0.1.

5. XRD Measurements

Following the analysis of Kaganer, the correlation factor and dislocation types are identifiable by the 004 and 224GE reciprocal lattice points. Symmetric Bragg scans of 004 peaks are shown in Figure 12 (a). The peak separation between the GaSb and GaAs peaks can be readily measured to be in the range of 9600", which corresponds to the expected value for a relaxed GaSb layer (9554"). Closer inspection of the GaSb peak in Figure 12 (b) shows that not only is the peak larger for thicker samples, but that the FWHM decreases with thickness as well. The higher peak is indicative of greater diffraction, which can be expected for thicker buffers. The wider peak corresponds to the broadening mechanism given by Kaganer. Furthermore, rocking curves of the GaSb 004 peak, as shown in Figure 12 (c), display a similar trend as the symmetric scans. Both peaks are expected to broaden with decreasing GaSb thickness in the correlation model.

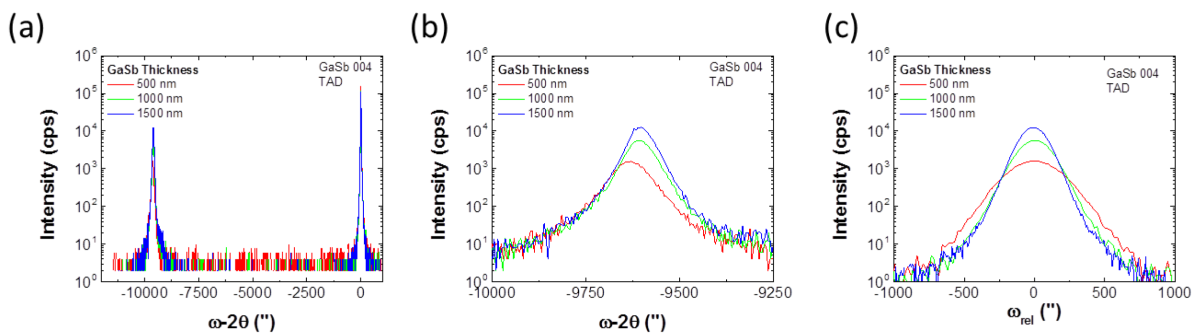

Figure 12: (a) Symmetric scan of GaAs (right) and GaSb (left) peaks. (b) GaSb peak from (a). (c) Rocking curve of GaSb 004 peak.

RSMs of the GaSb 224 GE reciprocal lattice point were taken for all four samples in order to compare to the expected results from Kaganer et al. The RSMs can be found in Figure 13. All peak intensities were normalized to the largest intensity for the sake of FWHM comparisons. The difference in the FWHM values for different thicknesses is immediately apparent, as is the similarity between the shape of the displayed values and RSMs displayed in Figure 11. The thicker samples behave much like the previous simulations, with the exception of tails in the $\mathbf{Q}_z$ direction. The tails are most likely a result of dynamical diffraction, and only serve to underscore the epitaxial quality of the film. The thinner samples show much broader FWHM values, and while their *ρd* far exceeds 1, it is not clear why this is so. However, the superelliptical shape of the RSM remains and the RSMs for the thicker samples do not show anisotropic broadening, which would be expected for 60° dislocations.

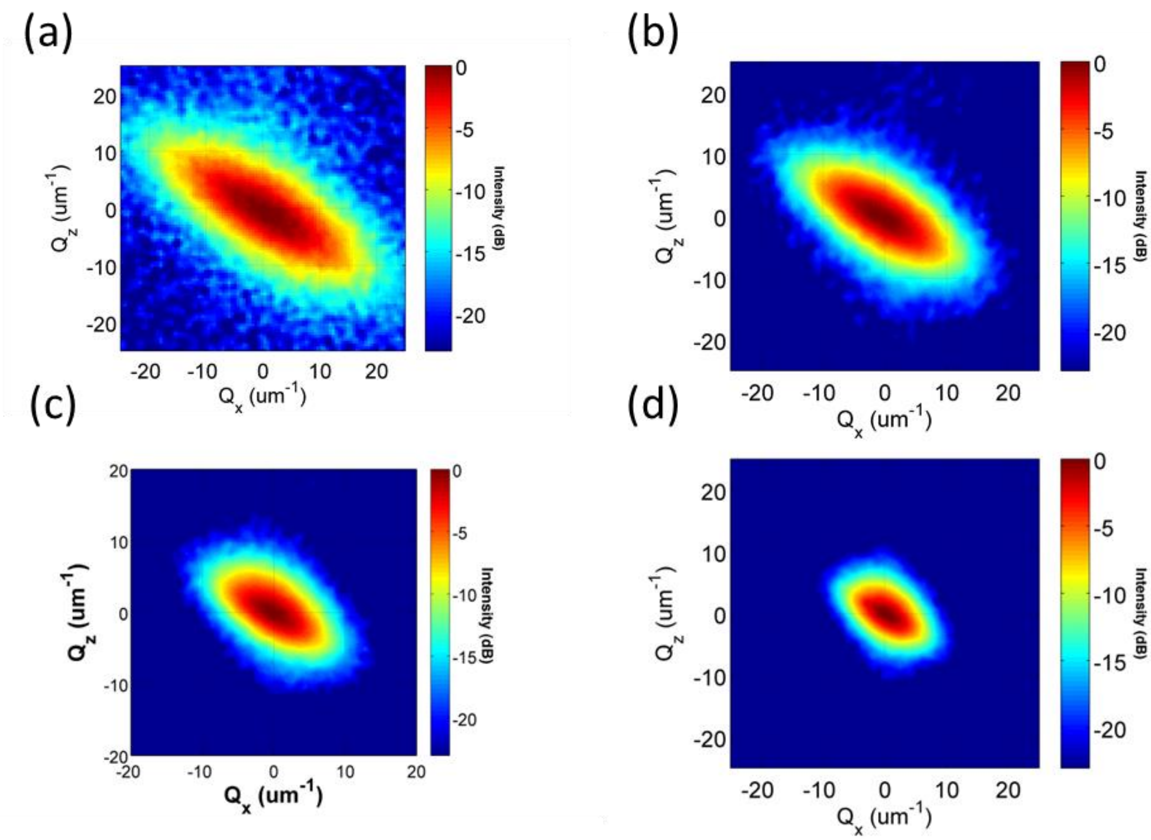

Figure 13: 224 GE RSMs of GaSb buffers with thicknesses of (a) 250 nm, (b) 500 nm, (c) 1 µm, and (d) 1.5 µm thickness.

6. XRD Fittings

In accordance with Kaganer, a simple method to determine the dislocation type is the angle ϕ of the 224GE RSM and the FWHM ratio for both the symmetric and rocking curves of the 004 RLP. The angle ϕ can be calculated by taking the FWHM in both the $\mathbf{Q_z}$ and $\mathbf{Q_x}$ direction and applying the tangent. Both of these are displayed in Figure 14, which also contains a plot of the relaxation versus GaSb thickness. The relaxation shows that the GaSb epilayer is 99.5% relaxed by the first 250 nm of growth. Previous estimations of the GaSb relaxation at the interface were on the order of 97.5%.[9] The epilayer continues to relax with further deposition, and does not fully relax even for the 1,500 nm thick buffer. While the introduction of further dislocations could cause the additional relaxation, the critical thickness for such relaxed material makes it unlikely.[10] Other processes, such as surface roughening, are possible, and measurements using tip-enhanced Raman spectroscopy should yield insights into the strain fields at the surface.[11,12] The angle ϕ shows a similar trend as the relaxation, shifting from 33° to almost 37°. The expected value for a 90° dislocation array is 38°. And finally, the GaSb 004 FWHM ratio between the $\mathbf{Q_z}$ and $\mathbf{Q_x}$ directions is expected to be 0.37 for 60° dislocation and 0.71 for 90° dislocation. The measurements once again show a thickness dependence, most likely indicative of the greater relaxation. The previous uses of this method – especially for GaAs on Si – also utilized thicker buffers that were more likely to have completely relaxed.[8]

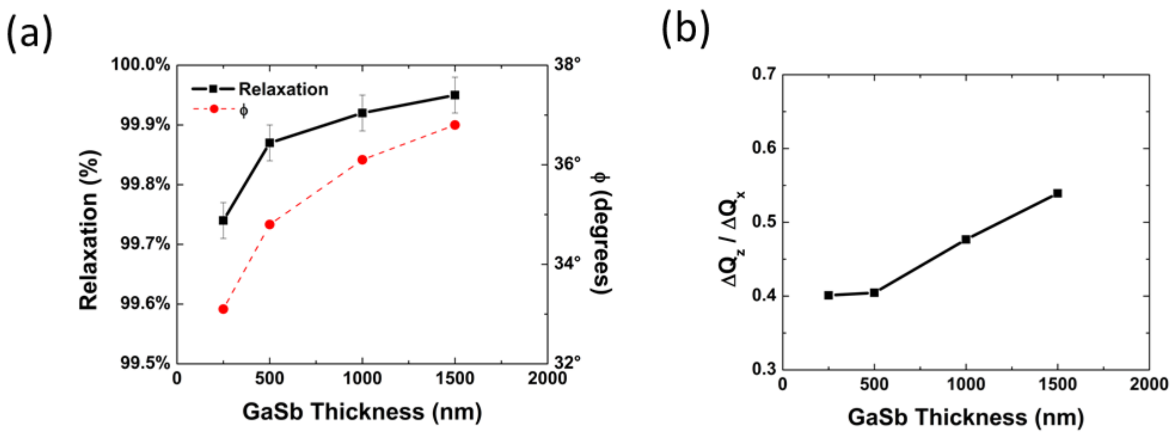

Figure 14: (a) Relaxation and angle of GaSb 224GE RLPs. (b) Change in GaSb 004 FWHM relationship with thickness.

The super-elliptical shape of the RSMs and the TEM analysis provide ample evidence that the IMF is largely forming, however more careful calculations of the correlation factor are possible using the FWHM values from the GaSb 004 RLP. The FWHM values and peak separations for the samples are summarized in Table 1.

Thickness	Peak	Q_z FWHM	Q_x FWHM
1,500 nm	-9,606”	60”	190”
1,000 nm	-9,615”	67”	240”
500 nm	-9,629”	90”	380”
250 nm	-9,667”	119”	507”

Table 1: XRD characteristics of IMF buffers

The FWHM values are converted from the measured units (arcsec) into reciprocal lattice units (μm^{-1}), where they are then multiplied by the thickness of the buffer layer. The results are plotted in Figure 15. Calculations for an uncorrelated 90° dislocation array are given as solid lines, and the dashed curves represent the best fit to the measured data. The dashed curves represent a correlation factor of 0.015 for the $\mathbf{Q}_x$ direction and a correlation factor of 0.005 for the $\mathbf{Q}_z$ direction. These values can be directly interpreted non-uniformity of approximately 1%, or an IMF array that is 99% perfect. Experimental error is assumed to be the cause of the slight discrepancy between the directions.

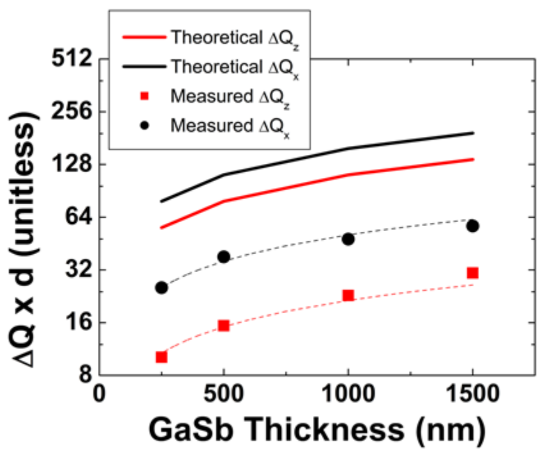

Figure 15: Curves for fitting to the correlation factor assuming a dislocation spacing of 5.6 nm. The dashed lines represent correlation factors of approximately 0.01.

7. Discussion

The model and the recent literature give some further insights into the cause of the broadening. The introduction of 60° threading dislocations, even at low densities, would drastically increase the FWHM values and create largely anisotropic RSMs. Furthermore, the deviation in the dislocation spacing is only 56 picometers, or less than the interatomic distance in the lattice. The most likely cause of the broadening is the existence of two 60° dislocations that form a dislocation loop very close to the interface. These dislocation loops have recently been found using an aberration corrected TEM and a plan-view sample.[13] While the introduction of these dislocation loops indicates that the IMF was not fully formed, a dislocation loop so close to the interface is not of major concern.

8. Conclusions

XRD analysis of IMF-based GaSb buffer layers was used to verify the existence and quality of a 90° dislocation array. The relaxation of the GaSb buffer was shown to increase with deposition, and the GaSb was over 99.5% relaxed at 250 nm thickness. The FWHM values were also very narrow (60" for 1.5 µm thick buffers), and could be used to extract the correlation factor of the IMF. The IMF was found to have between 0.5% - 1.5% variation. Possible sources of the variation include dislocation loops at the interface or effects of the model. The non-destructive verification of IMF quality is tantamount for characterization of IMF-based photodiodes.

9. References

[1] G. Balakrishnan, S. Huang, L. R. Dawson, Y. C. Xin, P. Conlin, and D. L. Huffaker, Applied Physics Letters **86** (3), 034105 (2005).

[2] A. Yu Babkevich, R. A. Cowley, N. J. Mason, S. Weller, and A. Stunault, Journal of Physics: Condensed Matter **14** (49), 13505 (2002).

[3] J. E. Ayers, Journal of Crystal Growth **135** (1–2), 71 (1994).

[4] Paul F. Fewster, Vaclav Holy, and Norman L. Andrew, Materials Science in Semiconductor Processing **4** (6), 475 (2001).

[5] P. B. Rago and J. E. Ayers, Journal of Electronic Materials, 1 (2013).

[6] V. M. Kaganer, R. Köhler, M. Schmidbauer, R. Opitz, and B. Jenichen, Physical Review B **55** (3), 1793 (1997).

[7] C. J. K. Richardson, L. He, and S. Kanakaraju, Journal of Vacuum Science & Technology B: Microelectronics and Nanometer Structures **29**, 03C126 (2011).

[8] V. M. Kaganer, A. Shalimov, J. Bak-Misiuk, and K. H. Ploog, Applied Physics Letters **89** (2), 021922 (2006).

[9] S. H. Huang, G. Balakrishnan, A. Khoshakhlagh, A. Jallipalli, L. R. Dawson, and D. L. Huffaker, Applied Physics Letters **88** (13), 131911 (2006).

[10] J. W. Matthews and A. E. Blakeslee, Journal of Crystal Growth **27** (0), 118 (1974).

[11] Y. Xie, G. Gilmer, C. Roland, P. Silverman, S. Buratto, J. Cheng, E. Fitzgerald, A. Kortan, S. Schuppler, M. Marcus, and P. Citrin, Physical Review Letters **73** (22), 3006 (1994).

[12] J. Tersoff and F. K. LeGoues, Physical Review Letters **72** (22), 3570 (1994).

[13] Yi Wang, P. Ruterana, S. Kret, S. El Kazzi, L. Desplanque, and X. Wallart, Applied Physics Letters **102** (5), 052102 (2013).

Chapter 4: GaSb *P-I-N* Photodiodes

1. Background

The homojunction GaSb photodiode is a poorly researched device. There are less than a dozen reports of GaSb or $Al_xGa_{1-x}Sb$ homojunction photodiode performance, most of which come to the conclusion that GaSb will never compete with $In_{0.53}Ga_{0.47}As$/InP based infrared detectors because of the high leakage currents.[1-5] As such, Phosphide-based photodiodes dominate high bandwidth markets for telecommunications, Laser Detection and Ranging (LADAR), and time-of-flight applications. However, lattice-matching conditions for the Phosphides limit them to 1.65 µm cut-off wavelengths, or approximately 2.5 µm using metamorphic growth. High bandwidth Antimonide photodiodes could potentially provide a solution, with lattice-matched cut-off wavelengths anywhere between 1.7 - 4.4 µm.

The best bandwidth performance in a $Al_xGa_{1-x}Sb$ photodiode was by Kuwatsuka et al. in 1990.[6] Kuwatsuka utilized the high impact ionization coefficients of $Al_{0.05}Ga_{0.95}Sb$ in order to create a device that could create higher gain than nascent InGaAs/InP technologies. The *RC*-limited response was 8 GHz for a 30 µm mesa, which was a direct result of high background doping concentration (6×10^{16} cm^{-3}) and subsequently high depletion capacitance (600 fF). Kuwatsuka was also limited by the avalanche build-up time of his devices. While the device capacitance decreased with reverse bias (increasing the *RC*-limited bandwidth), the multiplication factor and avalanche build-up time also increased. Thus, any attempts to modulate beyond 10 GHz were futile.

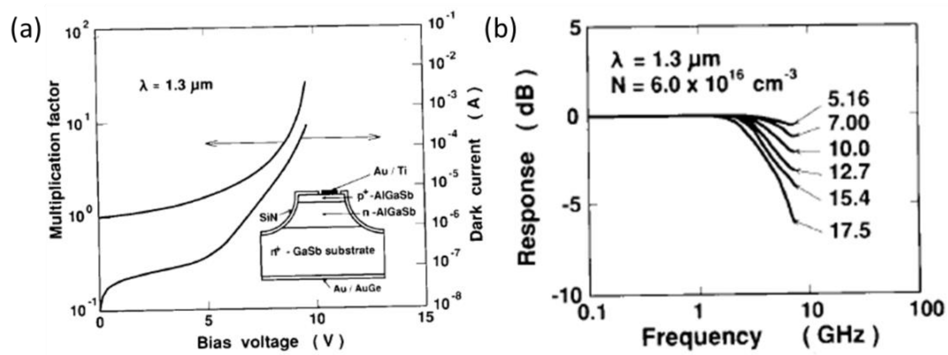

Figure 16: Previous attempts at high bandwidth AlGaSb diodes with APD multiplication. (a) IV curve and schematic. (b) Frequency response at given multiplications. From Kuwatsuka.[6]

An IMF-based, homojunction GaSb photodiode offers several advantages over its homoepitaxial counterpart. The first advantage is the use of mature, ohmic GaAs *n*-contacts. While ohmic *n*-contacts to GaSb have been reported, *n*-GaSb experiences Fermi-level pinning in the valence band at the surface.[7] This creates a very large barrier and high contact resistance. A typical response is to increase the contact area substantially by using the entire backside of the wafer (much like Kuwatsuka), but this also increases parasitic capacitance and leakage current from the substrate. A better alternative is placing co-planar waveguide contacts on a semi-insulating substrate (schematic shown in Figure 19). The second advantage for an IMF-based design is this semi-insulating substrate, which allows the placement of contacts without parasitic capacitance from the substrate. Semi-insulating GaSb substrates are generally unavailable and inferior to semi-insulating GaAs substrates. Furthermore, the large area of the substrate and high dielectric constant of GaAs (12.89) make it imperative to avoid accumulation of charges on the surfaces, as the addition of 10 fF can severely limit *RC* performance.

Homojunction diodes based on an IMF template are not only useful for bandwidth measurements, but also for fundamental material information. The variable depletion width in the *p*-region is useful for the measurement of trap density using admittance spectroscopy, and is enabled using the tellurium compensation doping. Also, the device geometry and optical response can be used to measure the surface recombination velocity, the IMF recombination velocity, and the minority carrier lifetime. These values are useful for future device modeling.

2. Acceptor Doping Compensation

The design of the photodiode was driven by several constraints. While most of these were driven by fabrication considerations – the thickness of the contact layers, the doping level in the contact layers, etc. – the key constraint for high bandwidth performance is the junction capacitance of the diode. The junction capacitance is given by the following equations:

$$V_{bi} = \frac{kT}{q} \ln\left(\frac{N_A \cdot N_D}{n_i^2} \right)$$

$$w_{depletion}(V) = \sqrt{\frac{2 \cdot \varepsilon_0 \varepsilon_{GaSb}}{q} \cdot \left(\frac{N_A + N_D}{N_A \cdot N_D} \right) \cdot (V_{bi} - V)}$$

$$C_{junction} = \frac{A \cdot \varepsilon_0 \varepsilon_{GaSb}}{w_{depletion}(V)}$$

In a one-sided junction (where $N_D >> N_A$), the capacitance is mostly controlled by the lower limit of N_A. Lower N_A values form larger depletion regions and therefore smaller junction capacitance values. Calculated curves for the *RC*-limited bandwidth are given in Figure 17. These show that not only does the bandwidth increase, but the sensitivity to reverse bias increases as well. The calculations assume a series resistance of 50 Ω, a load of 50 Ω, and a mesa diameter of 30 µm.

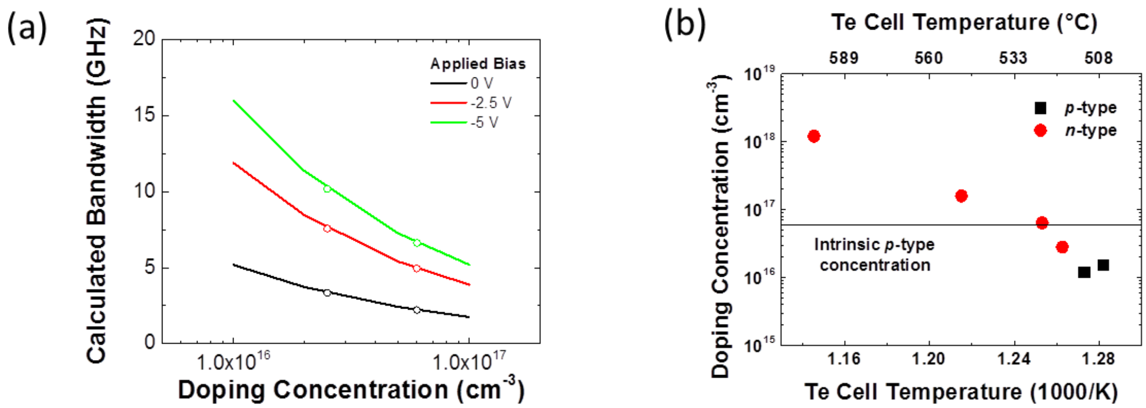

Figure 17: (a) RC Bandwidth for different N_a concentrations for 30 um diameter mesas. Circled points show as-grown GaSb (6 x 10^{16} cm^{-3}) and Te compensation-doped structures (2.5 x 10^{16} cm^{-3}). (b) Donor concentration in IMF-based GaSb by Tellurium cell temperature. Note the change from p-type to n-type over approximately 6.5°C in Tellurium cell temperature.

The background acceptor concentration of GaSb is typically in the 10^{16} – 10^{17} cm^{-3} range, which would limit the overall bandwidth of the device. A series of 1 µm thick IMF-based GaSb buffers were grown for room temperature Hall measurements. The variable was the Tellurium cell temperature, which was varied from the equivalent donor concentrations of 10^{15} cm^{-3} to 10^{18} cm^{-3}. The relationship between Tellurium cell temperature and measured doping concentration is given in Figure 17 (b).

The change from *p*-type to *n*-type occurred over a 6.5°C change in cell temperature, and the Tellurium doping Arrhenius plot exhibits three distinct slopes: (1) high donor concentration, (2) low donor concentration, and (3) low acceptor concentration. The minimum doping concentration reached was an acceptor concentration of 1.2 x 10^{16} cm^{-3}. While prior research has indicated that the primary risk with Tellurium compensation doping is a loss of carrier mobility, the mobility of each sample was over 1,000 cm^2 per Volt second, almost identical to the undoped samples.[8]

3. Fabrication

The final device structure is given in Figure 18. The sample was grown on a semi-insulating GaAs substrate using a solid-source molecular beam epitaxy reactor. Arsenic and antimony are both cracked using standard valved crackers. The V/III ratio for GaAs is approximately 10, the growth temperature

580°C, and the growth rate 1 ML/sec. After growth of the n-GaAs contact, an IMF array is formed, the growth temperature is lowered to 510˚C, and the GaSb layers are grown at a growth rate of 1 ML/sec and beam equivalent flux V/III ratio of 4.2. The details of the IMF growth mode are found in Huang et al.[9] The GaAs is *n*-doped with Si, the GaSb is *n*-doped with GaTe, and the GaSb *p*-dopant is Be. The 1 µm intrinsic region is compensated doped with Tellurium and the cell temperature is 512.5°C.

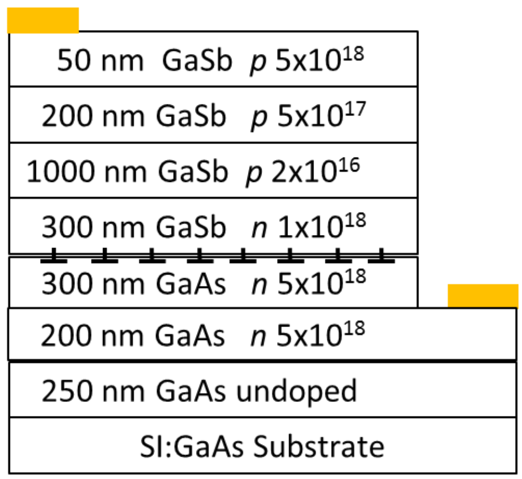

Figure 18: Final device structure for high bandwidth photodiode.

High-bandwidth devices are fabricated using standard photolithography and dry etching. First, a top Ti/Pt/Au contact is e-beam evaporated onto the epitaxial surface. Then, the photodiode mesas are etched using an ICP RIE etch and BCl_3/Ar etch chemistry. Following the dry etch, HCl:H_2O_2: H_2O is used as a clean-up dip. Then, an AuGe/Ni/Au contact is deposited on n-GaAs. The samples are annealed at 315˚C for 20 sec to ensure ohmic contacts. A secondary isolation mesa is then etched using the same BCl_3 chemistry, exposing the semi-insulating GaAs substrate. PMMA is used to create an air bridge support, then a layer of Ti/Au is deposited to form the ground-signal-ground contact pads on the semi-insulating substrate. The PMMA support is left in place during measurements and the samples are unpassivated. A scanning electron microscope image of a fabricated photodiode with an air bridge (dark ridge) is shown in Figure 19 (center). A range of mesa diameters is included in the design (10 – 50 µm). A second set of devices that did not include the isolation etch or ground-signal-ground contact pads was also fabricated for process debugging, and featured larger diameter mesas for responsivity measurements (50 – 800 µm).

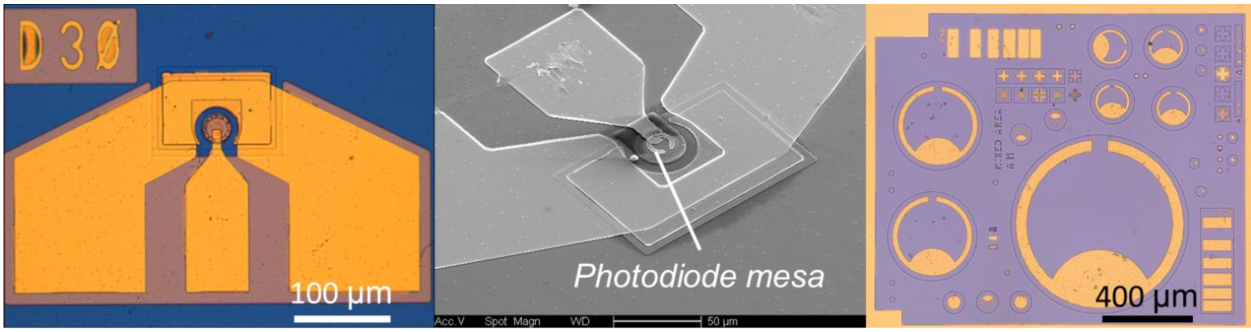

Figure 19: Different contact layouts from left to right. Optical microscope image of high bandwidth mask with co-planar waveguide on semi-insulating substrate (left). SEM of air-bridge (dark region to upper left of photodiode mesa) showing metal continuity (center). Optical microscope image of mixed area mask for process development (right).

4. Room Temperature Characteristics

The room temperature electrical characteristics of the device are measured using an Agilent E4980A LCR meter and an Agilent 4156C parameter analyzer. These results are seen for multiple device diameters in Figure 20 (a), and several points can be highlighted. First, the dark current densities shown here (10^{-2} to 10^{1} A/cm^2) are similar in magnitude to homojunction devices reported in the literature.[1,4,5] Second, the ideality factors of the devices are in the 1.8-1.9 range. These values indicate that the dark current originates from generation-recombination mechanisms in the depletion region, and are not diffusion limited. Third, the *RC*-limited behavior of the devices is promising. All of the diodes exhibit R_{series} less than 30 Ω, as calculated from a diode fitting algorithm. Furthermore, the capacitance is low because of the acceptor doping compensation. The 30 µm diameter device has a capacitance of 111 fF at -5 V, which corresponds to an *RC*-limited frequency response of 20.5 GHz. The dark current for such a device is 40.3 µA at -5 V, which does not match state-of-the-art $In_{0.53}Ga_{0.47}As$. Finally, the poor *C-V* fit at low bias is most likely indicative of Fermi-level pinning. Fermi-level pinning is verified from the calculated built-in potentials, which are 0.2-0.3 V, as opposed to the modeled 0.6 V. It is unclear where the Fermi-level is pinned from the smaller diameter devices.

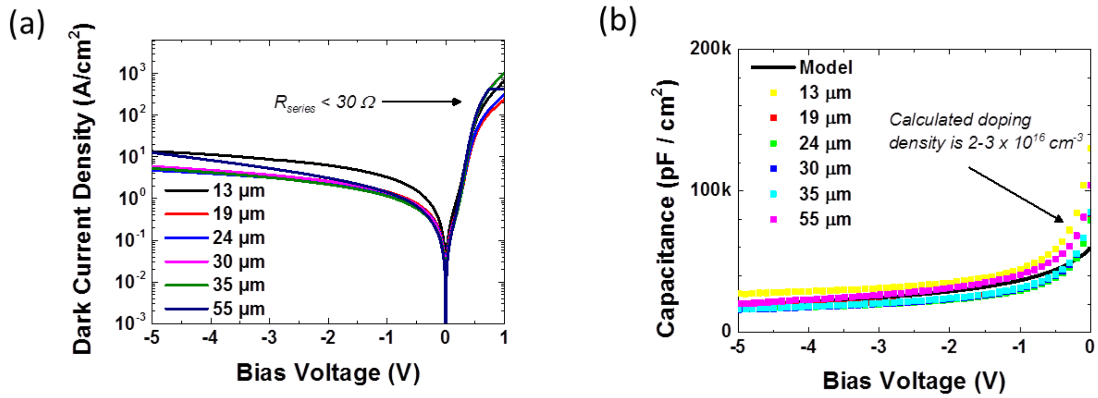

Figure 20: (a) *J-V* characteristics of multiple mesa sizes. Note the low series resistance. (b) *C-V* plot of multiple mesa sizes. Note the similarity to the modeled 2.5 x 10^{16} cm^{-3} *C-V* curve.

5. Bandwidth Measurements

The frequency response of the devices are measured using a vector network analyzer, a 1.55 µm laser, and an electro-absorption modulator driven by a variable RF source. The wavelength restricted absorption to the GaSb region, and approximately 80% of the optical power is absorbed in a single pass. The components are individually calibrated to allow correction for the system loss, in conjunction with calibration data for the modulator. The measured frequency responses show a dependence on mesa area, as seen in the Figure 21. For larger 55 µm diameter diodes, the 3 dB cut-off frequency is 6 GHz, which increases to approximately 20 GHz for 30 µm diameter photodiodes. Since these devices were not impedance-matched to the 50 Ω system, the frequency response results included a ripple that is superimposed on the fundamental photodiode response. The bandwidth is over two times the previous record by Kuwatsuka.[6]

The diodes' frequency responses are compared to predicted *RC*-limited responses, using measured R_{series} and C values from each photodiode. This is shown in Figure 21. The good fit across different diode areas confirms that the measured bandwidths are *RC*-limited by the contacts and junction capacitance, not transit time. The transit time bandwidth is estimated to be greater than 40 GHz for a 600 nm depletion region, which corresponds to the depletion at -5 V. While the saturation velocity of GaSb has never been measured experimentally, calculations and simulations indicate that the value lies between 10^6-10^7 cm/sec.[10,11] The saturation velocity is assumed to be 5 x 10^6 cm/sec in this instance.

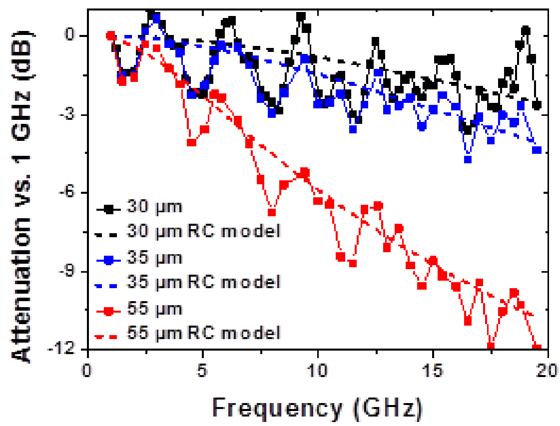

Figure 21: Frequency response of three photodiodes of different mesa size. The modeled RC response from IV fittings and CV data is shown, indicating that the bandwidth limitation is from the junction capacitance and contact resistance.

6. *I-V* vs. Temperature Measurements

The bandwidth of the device is impressive, but further reduction of the leakage current is necessary to compete with $In_{0.53}Ga_{0.47}As/InP$ photodiodes with a similar bandgap. Calculations of the diffusion current, based on the fabricated device, indicate that the leakage current density could be as low as 1-5 x 10^{-6} A/cm^2. The assumed variables are carrier lifetimes of 1-10 nanoseconds, electron mobilities of 1,900 cm^2 per Volt second, and hole mobilities of 400 cm^2 per Volt second. Possible sources of leakage current include Shockley-Read-Hall recombination, Auger recombination, and surface recombination on either the sidewalls or the top of the mesa.

Key insights into the recombination schemes can be done by using temperature-dependent measurements of *I-V*. A representative curve for a 100 µm diameter mesa is shown in Figure 22 (a). The curve exhibits several trends. First, the leakage current decreases with decreasing temperature, as expected, from 0 V to -8 V. The changes in leakage are not very large, which is surprising. Differences of an order of magnitude or more are common for almost all semiconductors, whether they have low bandgaps or high bandgaps.[12,13] Second, the leakage increases with decreasing temperature from -8 V to -12 V. This behavior is indicative of avalanche gain.[13] The breakdown voltage (defined here as the largest change in d*J*/d*V*) is plotted in the adjacent figure. The slope of the breakdown voltage is 8 mV/K, which compares favorably to GaAs for the same depletion region, and is the only known measurement of the temperature dependence of GaSb breakdown.[14]

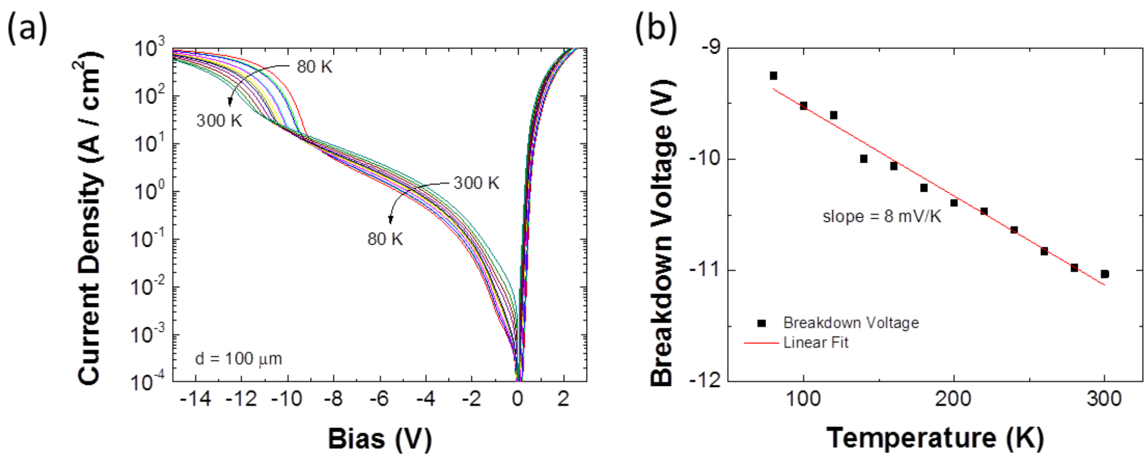

Figure 22: (a) Dark *J-V* vs. T for a 100 μm diameter device. (b) Plot of breakdown voltage vs. T based on the measured data.

7. *C-V* vs. Temperature Measurements and Admittance Spectroscopy

A second set of techniques to characterize the source of leakage utilizes *C-V* vs. temperature measurements. These are perhaps the most highly researched techniques for determining trap concentration, activation energy, and cross section. Seminal contributions to this field were from C. T. Sah et al., who demonstrated that thermally stimulated capacitance (TSCAP) measurements could be used to calculate all trap parameters.[15] Sah's method was simple, in that it required a single oscillation frequency (typically 1 MHz), but that it had limited ability to measure traps with activation energies below 250 meV and had trouble differentiating between trap states. Time and frequency dependent techniques were therefore needed. D. V. Lang demonstrated how to measure deep-level traps with deep-level transient spectroscopy (DLTS).[16] This technique utilized a pulsed system to fill and empty traps, thereby allowing users to directly calculate the capture and emission cross sections. Furthermore, by using capacitance vs. time measurements after the pulse, it was possible to measure extremely low emission rates of deep levels. Unfortunately, DLTS required non-standard characterization equipment, including a pulse source, high-speed capacitance meter, and boxcar analyzer. D. Losee provided an answer to these problems with admittance spectroscopy.[17] This technique only requires an LCR meter with variable frequency measurement capability.

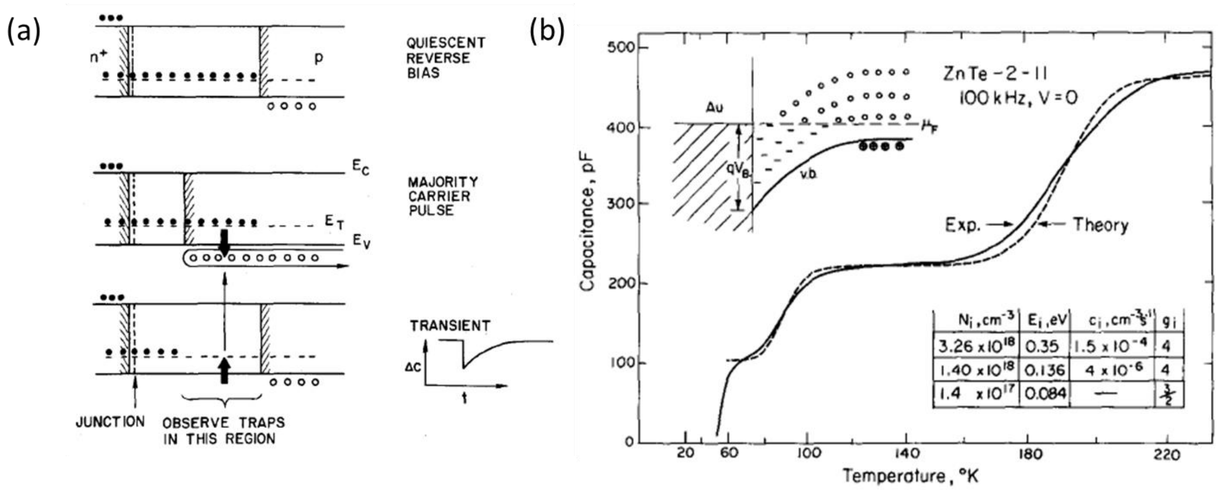

Figure 23: (a) Theory of operation of DLTS from Lang.[16] (b) Theory of operation of admittance spectroscopy from Losee.[17]

The physical principal behind all three trap characterization techniques is moving the Fermi level in the junction through the trap state. Begin with a deep-level acceptor state and place it directly in the middle of the bandgap. Now, assume that the region is *p*-doped and that the depletion through the region is governed by either a Schottky barrier or a one-sided *p-n* junction. When the state is in the neutral regions, it will be filled by a hole as it resides above the Fermi-level. However, when it resides in the space-charge region, the state will be below the Fermi-level and will emit the hole at a rate determined by the cross section and activation energy. If more information regarding the depletion width is known, a careful estimate the trap concentration can be determined based on changes in the *C-V*. The capture and emission of carriers will be detected during a capacitance measurement, as more charges will be able to couple to the oscillating field. The diode can be modeled as a parallel *RC* circuit.

The admittance spectroscopy technique focuses on changes in the shunt conductance (*G,* or *1/R*) of the diode with frequency (ω). A conductance peak is expected whenever the Fermi level crosses the trap state's energy. As the conductance is temperature and frequency dependent, the peak temperature changes with temperature and can be plotted on an Arrhenius plot to calculate activation energy.

The *C-V* of several devices was measured across a range of frequencies (20 kHz, 40 kHz, 100 kHz, 200 kHz, 400 kHz, and 1 MHz) as well as various temperatures (80 – 320 K by 5 K increments) to determine the location of the traps using either TSCAP or admittance spectroscopy. Furthermore, a set of modeled curves were generated based on changes to the intrinsic carrier concentration with temperature. The *C-V* curves at 1 MHz oscillation frequency are shown in Figure 24 (a), alongside the modeled curves. The measured values match the modeled curves values fairly closely from 100 K to 300 K, indicating that no trap-state could be identified with TSCAP at a single frequency. However, the built-in potential across different mesa diameters (calculated using a linear regression of $1/C^2$ vs. voltage) did exhibit trap-like behavior. At high frequencies, all mesa diameters behaved similarly. Since high frequencies correspond to high emission rates and low activation energies, the possibility of a low activation energy trap at the sidewall can be eliminated. However, as the oscillation frequency was lowered, differences between the built-in potential became evident across mesa diameters. These differences disappeared as the sample was cooled, which corresponds with the expected result for a deep-level sidewall state. Unfortunately, there are no viable theories for *C-V* measurements of sidewall states, making it impossible to determine the trap activation energy or cross section from this measurement.

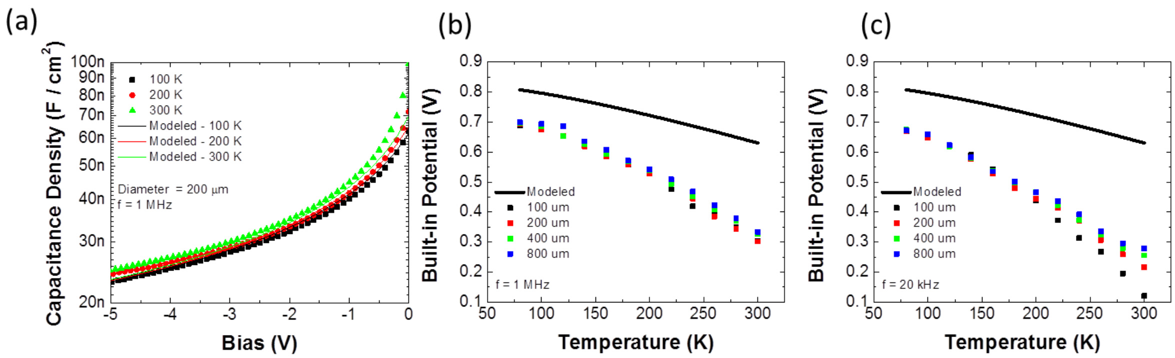

Figure 24: (a) *C-V* vs. 100 K, 200 K, and 300 K, as well as modeled changes to the curve. (b) Built-in potential of various mesa diameters measured at 1 MHz. (c) Built-in potential of various mesa diameters at 20 kHz.

The built-in potential measurement indicated that the sidewalls were able to deeply pin the Fermi-level at high temperatures, however this measurement does not indicate the existence of a deep-level state in the bulk. An admittance spectroscopy plot was generated based on the measured frequencies for a 400 µm diameter device. The plots for both -1 V and -2 V are displayed in Figure 25 (a) and (b), respectively. The admittance spectroscopy plots show a straight line with no peaks from 80 K to 320 K, indicating that a deep-level acceptor state was unlikely.

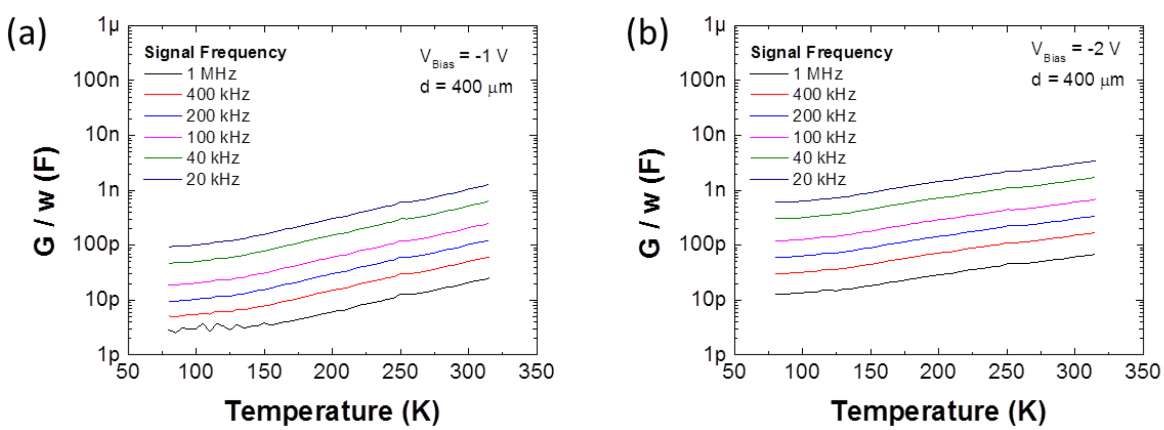

Figure 25: Admittance spectroscopy plots at both -1 V (a) and -2 V (b). Neither plot exhibits a peak, indicating that any hole traps are very shallow (<150 meV) or deep (>500 meV).

8. Lifetime Measurements

The carrier lifetime of the GaSb region can also be determined using optical excitation techniques, if several variables are known.[18] The equations provide a framework by which to measure the front surface recombination velocity, the carrier lifetime, and the back surface recombination velocity if other parameters are known. The equations are:

$$J_{scr} = q\phi(1-R)\exp(-\alpha x_j)(1-\exp(-\alpha W_d))$$

$$J_n = \left[\frac{q\phi(1-R)\tau_n}{\alpha^2 L_n^2 - 1}\right]\left[\frac{\left(\frac{S_n L_n}{D_n} + \alpha L_n\right) - \exp(-\alpha x_j)\left(\frac{S_n L_n}{D_n}\cosh\left(\frac{x_j}{L_n}\right) + \sinh\left(\frac{x_j}{L_n}\right)\right)}{\frac{S_n L_n}{D_n}\sin\left(\frac{x_j}{L_n}\right) + \cosh\left(\frac{x_j}{L_n}\right)} - \alpha L_n \exp(-\alpha x_j)\right]$$

$$J_p = \left[\frac{q\phi(1-R)\alpha L_p}{\alpha^2 L_p^2 - 1}\right]\exp(-\alpha(x_j - W_d)$$

$$\times\left[\alpha L_p - \frac{\left(\frac{S_p L_p}{D_p}\right)\left[\cosh\left(\frac{H'}{L_p}\right) - \exp(-\alpha H')\right] + \sinh\left(\frac{H'}{L_p}\right) + \alpha L_p \exp(-\alpha H')}{\frac{S_p L_p}{D_p}\sinh\left(\frac{H'}{L_p}\right) + \cosh\left(\frac{H'}{L_p}\right)}\right]$$

Equation 2: Equations governing photocurrent in a *p-n* junction

The sum of all three equations is the overall photocurrent generated by the device for an optical flux ϕ. The other variables are: *R*, the reflectivity; *α*, the absorption coefficient at each wavelength; W_d, the width of the depletion region; *H'*, the distance from the IMF to the edge of the depletion region; x_j, the distance from the front surface of the mesa to the depletion region; L_p and L_n, the diffusion lengths of the minority carriers; and D_p and D_n, the diffusion coefficients of the minority carriers. The remaining values to solve for are the front surface recombination velocity (S_p), the IMF recombination velocity (S_n), and the minority carrier lifetimes (τ_n and τ_p). The minority carrier lifetimes are assumed to be identical, as per convention. Other necessary variables for accurate modeling include the electron and hole mobility (1,900 cm^2 per Volt second and 400 cm^2 per Volt second, respectively), the DC permittivity (15.7), and the intrinsic carrier concentration (1.7 x 10^{12} cm^{-3}). The carrier mobilities were taken directly from Hall measurements, while the DC permittivity and intrinsic carrier concentration were taken from the literature, as were the refractive indices and absorption coefficients for GaSb, shown in Table 2. The widths of the front region, depletion region, and back region were based on the doping levels in the *p-i-n* junction at zero bias.

Wavelength	Refractive Index	Absorption Coefficient
659 nm	4.6	1.6334×10^{7} cm^{-1}
1064 nm	3.9	2.8065×10^{6} cm^{-1}
1324 nm	3.8	1.7494×10^{6} cm^{-1}

Table 2: Optical properties of GaSb

The accurate calculation of minority carrier lifetime and recombination velocities requires that several assumptions be met. The first assumption is that at least three different wavelengths must be tested in order to provide a single answer for the three variables. The second assumption is that each wavelength should provide as large of a change in the absorption profile as possible, without causing undue complication from back reflections at the IMF interface. The calculated absorption profile is shown in Figure 26 (a). The wavelengths provide a large degree of coverage between complete absorption in the upper cladding layer (659 nm), to absorption across the entire GaSb region (1064 nm and 1310 nm). The 1310 nm laser is mostly absorbed by the GaSb/GaAs interface (95%), however only a very small percentage is reflected back because of the small refractive index difference between GaAs and GaSb (<10% reflected). The final assumption is that the photoresponse is linear, and that other physical effects do not dominate. This can be verified by changing the incident laser power and measuring the corresponding changes in the photocurrent. As shown in Figure 26 (b), the photocurrent exhibits a linear response to changes in the incident optical power. Another measurement was done to verify the responsivity across various diameter devices. This measurement indicated that sidewall recombination did not play a role in the photocurrent calculation. Measured photocurrent values from each wavelength and optical power were then chosen.

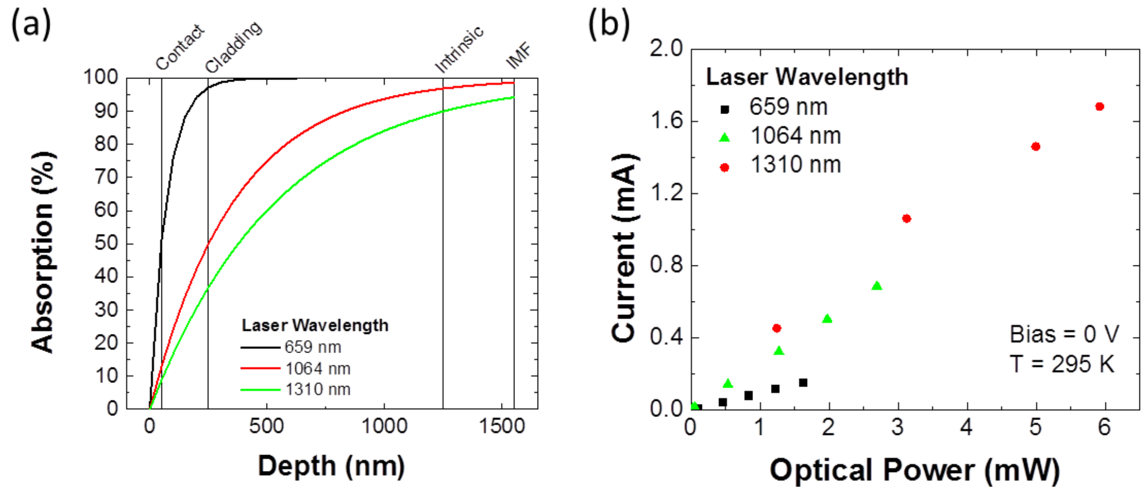

Figure 26: (a) Calculated absorption profiles for the diode. (b) Measured photocurrents vs. optical power for all three wavelengths.

The measured values were integrated into Matlab to solve for the front surface recombination velocity (S_p), the back surface recombination velocity (S_n), and the carrier lifetime (τ). The error was quantified by making 10% variations to the carrier mobilities and 50% variations to the doping concentration in the intrinsic region. The lifetime and surface recombination velocities were most sensitive to these parameters, and the values represent normal variations in the measurements. The front surface recombination velocity was $(1.6 \pm 0.2) \times 10^6$ cm/s and the lifetime was 440 ± 40 ps. The back surface recombination velocity was more difficult to quantify, but it appears to have a negligible effect on the external quantum efficiency. A series of recombination velocities were tested until an upper limit of 10^4 cm/sec was determined.

The lifetime presented here is approximately 4-5 times lower than what has been measured previously in GaSb devices, however it is well within the 100 ps to 16 ns range given for GaSb devices.[4] However, the recombination mechanism appears to be the same. GaSb's radiative and Auger lifetimes are considerably longer than 10 ns, leaving only SRH as a possible culprit. Furthermore, SRH recombination in GaSb has been a problem for almost all GaSb based devices, including superlattice structures.[19,20] SRH recombination is typically described by a mid-gap level defect state, which would normally be quantified using temperature dependent measurements.

9. Repeatability

The IMF is often questioned for its repeatability in devices. While structural characterization, such as the XRD technique explained in Chapter 3, are often given as examples for the absolute repeatability of the device, these techniques do not always capture the electronic component of the crystal. In order to full understand the repeatability of the IMF and its effects on devices, a second device was grown and fabricated two years after the first. During this time, the MBE growth chamber was vented three times (Spring 2011, Spring 2012, and Fall 2012). Each vent was accompanied by new source material (both gallium and antimony), as well as the removal of the substrate heater mount. That being said, the samples were grown under virtually identical conditions, and utilized RHEED grow rate measurements and substrate temperature calibrations in order to produce almost identical structures. After growth, the same masks and fabrication steps were used. Results from temperature dependent *I-V* and room temperature *C-V* are shown in Figure 27. The *I-V* measurements are within the expected error across the entire 200 K range, indicating that any traps have not changed. Furthermore, the *C-V* curves overlap almost exactly, indicating that the doping, junction, and Fermi-pinning are identical, which can be further verified by the similar ideality factors of the junctions. The only major difference between the samples is a change in the series resistance at 0.5 – 1.0 V. All contacts were verified to be ohmic, and the change in series resistance is mostly likely due to changes in the fabrication, specifically e-beam evaporation conditions and rapid thermal annealing.

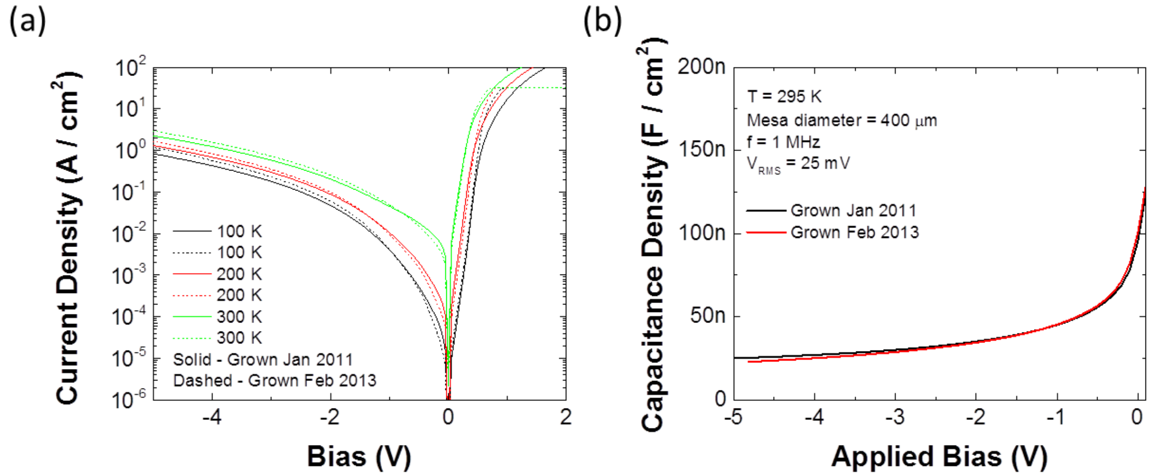

Figure 27: (a) *I-V* vs. Temperature for photodiodes grown over two years apart. (b) *C-V* at room temperature for two photodiodes.

10. Conclusion

The *p-i-n* photodiode measured here represents the highest bandwidth photodiode ever made using a GaSb or $Al_xGa_{1-x}Sb$ absorption region. The key innovations in this design include tellurium compensation doping, the use of a semi-insulating GaAs substrate for minimum parasitic capacitance, and the use of a low impedance, ohmic *n*-GaAs contact. The leakage current value was within an order of magnitude of homoepitaxial GaSb photodiodes, but more than 10^5 times greater than $In_{0.53}Ga_{0.47}As$/InP photodiodes with the same cut-off wavelength. The cause of the leakage is believed to be a deep level state on the sidewall that leads to a 440 ± 40 ps SRH lifetime. Unfortunately, no defect level could be identified using admittance spectroscopy. Further investigation of defect levels in GaSb and IMF-based GaSb will be necessary in order to determine the origins of the low lifetime.

11. References

[1] Sujatha Sridaran, Ashonita Chavan, and Partha S. Dutta, Journal of Crystal Growth **310** (7–9), 1590 (2008).

[2] G. Stollwerck, O. V. Sulima, and A. W. Bett, Electron Devices, IEEE Transactions on **47** (2), 448 (2000).

[3] E. K. Duerr, M. J. Manfra, M. A. Diagne, R. J. Bailey, J. P. Donnelly, M. K. Connors, and G. W. Turner, Applied Physics Letters **91** (23), 231115 (2007).

[4] A. Y. Polyakov, M. Stam, A. G. Milnes, and T. E. Schlesinger, Materials Science and Engineering: B **12** (4), 337 (1992).
[5] A. G. Milnes and A. Y. Polyakov, Solid-State Electronics **36** (6), 803 (1993).
[6] H. Kuwatsuka, T. Mikawa, S. Miura, N. Yasuoka, T. Tanahashi, and O. Wada, Photonics Technology Letters, IEEE **2** (1), 54 (1990).
[7] P. S. Dutta, H. L. Bhat, and Vikram Kumar, Journal of Applied Physics **81** (9), 5821 (1997).
[8] P. S. Dutta, V. Prasad, H. L. Bhat, and Vikram Kumar, Journal of Applied Physics **80** (5), 2847 (1996).
[9] S. H. Huang, G. Balakrishnan, A. Khoshakhlagh, A. Jallipalli, L. R. Dawson, and D. L. Huffaker, Applied Physics Letters **88** (13), 131911 (2006).
[10] P. Damayanthi, R. P. Joshi, and J. A. McAdoo, Journal of Applied Physics **86** (9), 5060 (1999).
[11] H. Hillbrand, physica status solidi (a) **5** (2), K113 (1971).
[12] Ker Pin Jern, A. R. J. Marshall, A. B. Krysa, J. P. R. David, and Tan Chee Hing, Quantum Electronics, IEEE Journal of **47** (8), 1123 (2011).
[13] C. Groves, R. Ghin, J. P. R. David, and G. J. Rees, Electron Devices, IEEE Transactions on **50** (10), 2027 (2003).
[14] Xie Shiyu and Tan Chee Hing, Quantum Electronics, IEEE Journal of **47** (11), 1391 (2011).
[15] C. T. Sah, W. W. Chan, H. S. Fu, and J. W. Walker, Applied Physics Letters **20** (5), 193 (1972).
[16] D. V. Lang, Journal of Applied Physics **45** (7), 3023 (1974).
[17] D. L. Losee, Applied Physics Letters **21** (2), 54 (1972).
[18] Simon M. Sze, Physics of Semiconductor Devices. (John Wiley & Sons, New York).
[19] Alexandre Laurain, Jörg Hader, Yi-Ying Lai, Tsuei-Lian Wang, Mike Yarborough, Ganesh Balakrishnan, Thomas J. Rotter, Pankaj Ahirwar, and Jerome V. Moloney, 82420S (2012).
[20] E. H. Steenbergen, B. C. Connelly, G. D. Metcalfe, H. Shen, M. Wraback, D. Lubyshev, Y. Qiu, J. M. Fastenau, A. W. K. Liu, S. Elhamri, O. O. Cellek, and Y. H. Zhang, Applied Physics Letters **99** (25), 251110 (2011).

Chapter 5: Interface Charge Density and Band Offsets

1. Background

Interfacial charge density and carrier redistribution at a heterointerface is an often overlooked aspect of semiconductor device engineering, yet plays an important role in the ultimate device performance.[1] Historically, studies of interface charge have focused on unipolar devices, where the charge density and carrier redistribution can be probed using field-effect transistors or semiconductor-insulator-semiconductor capacitors.[2] Major improvements in the transconductance have been accomplished in field effect transistors by close understanding of the charge carrier distribution and densities.[3] Meanwhile, bipolar devices have typically utilized C-V profiling techniques to calculate interface charge and carrier redistribution. Early demonstrations calculated both the band alignment and interface charge density in GaAs/AlGaAs heterostructures utilizing standard C-V measurements at a single frequency based upon either experimental or *a priori* knowledge of the doping concentrations, as shown in Figure 28 (a).[4] Further work on the spatial and energy distribution of charges was accomplished using transient measurements[5] (deep-level transient spectroscopy) and multi-frequency[6] (admittance spectroscopy) approaches. The band alignments, charge densities, and carrier distributions for InGaP/GaAs[7], InGaAs/InP[8], Si/SiGe[9] and GaAs/Si[10] heterointerfaces were all calculated in lattice-matched or lightly strained thin films.

Meanwhile, research on highly lattice-mismatched materials (>4% strain) has focused mostly on materials attributes of the heterointerface, specifically dislocation formation[11], propagation[12], and early termination[13]. Metamorphic buffers have become a standard approach to this problem. These structures typically utilize the substrate only as a mechanical platform, eliminate dislocations over several microns of growth, and do not seek to pass current through the metamorphic or dislocated region.[14] Many examples exist for both unipolar and bipolar InAs[15], GaSb[16], and InP-based[17] devices. An alternative approach to highly lattice-mismatched growth is an IMF. Both GaSb/GaAs[18] and GaSb/GaP[19] IMFs have been realized with dense Lomer dislocation networks in the range of 10^{12} cm^{-2}. However, the introduction of these dislocations – and the corresponding gallium dangling bonds – has long been suspected of producing extremely high interface acceptor densities (>$1x10^{12}$ cm^{-2}) in comparison to typical densities ($5x10^{10}$ – $5x10^{11}$ cm^{-2}) found in lattice-matched heterointerfaces.[20] Unfortunately, a direct measurement of the interface charge density has not been realized.

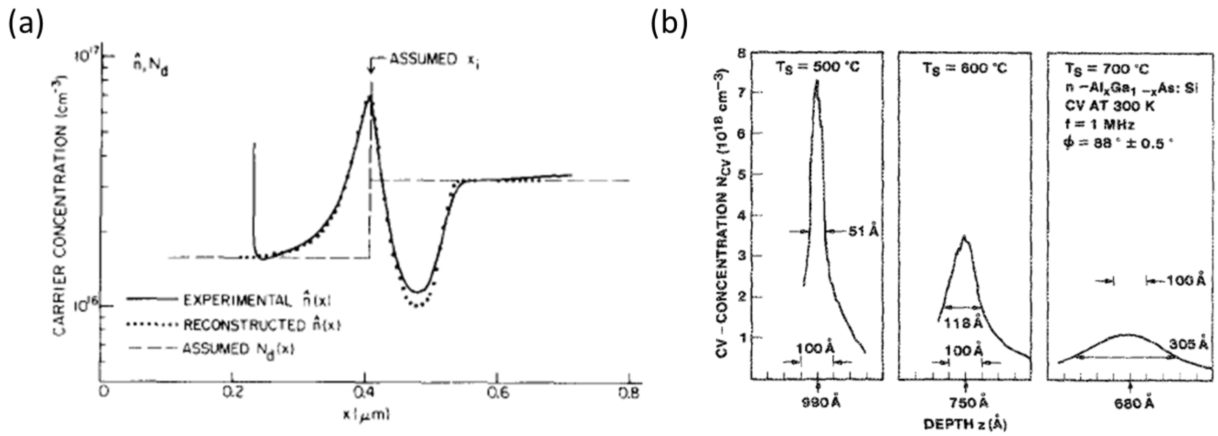

Figure 28: (a) Example of isotype heterojunction *C-V* profiling from Kroemer.[4] (b) Diffusion of Si delta-doping in AlGaAs from Schubert.[21]

A method of verification is necessary in order to determine if the *C-V* profile technique was performed properly. Delta-doping the GaAs side of the IMF with Silicon provides a reasonable option for verification. Choosing the GaAs side is important, as the first 20 nm of GaSb growth are not planar and dopant redistribution would be difficult to deconvolve. Furthermore, Silicon has two principal advantages over the other available dopant sources, Beryllium and Tellurium. A sheet of Beryllium acceptors will impede depletion through the IMF, making it more difficult to accurately determine its interface charge density. Meanwhile, Tellurium is not considered a good dopant for GaAs. While the sticking coefficient is very high, Tellurium tends to float on the surface of GaAs and incorporate randomly. Silicon is able to maintain very narrow profiles, even in the presence of diffusion (see Figure 28 (b)).[21]

2. Experimental Design

The measurement of interface charge density via isotype heterojunction *C-V* profiling imposes several constraints on the device design. The first constraint is the need to maintain a large difference (10^2) in doping concentration between the *n+* and *p-* sides of the junction. Without such a large difference, the once-sided junction model for doping concentration becomes invalid, complicating interpretation. Since the donor dopant source, silicon, has a maximum concentration of approximately 6-8 x 10^{18} in GaAs, and good ohmic contacts can be formed at concentrations above 1 x 10^{18} cm^{-3}, the doping concentration was chosen to be 2 x 10^{18} cm^{-3}. The second constraint was to maintain the depletion front of the junction in the GaAs region at low bias values. Doing so enables direct CV measurement of the *p*-GaAs doping. The third constraint was to deplete the GaAs region by -3 V. Higher reverse biases cause higher leakage, which can potentially limit the accuracy of CV measurements. The final structure is seen in Figure 29, and a schematic of the delta-doped devices is also included. The introduction of delta-doping within a Debye length of the IMF (and approximately the diffusion width away from the IMF) is used as both a marker to calibrate the charge density and as a manner to control depletion.

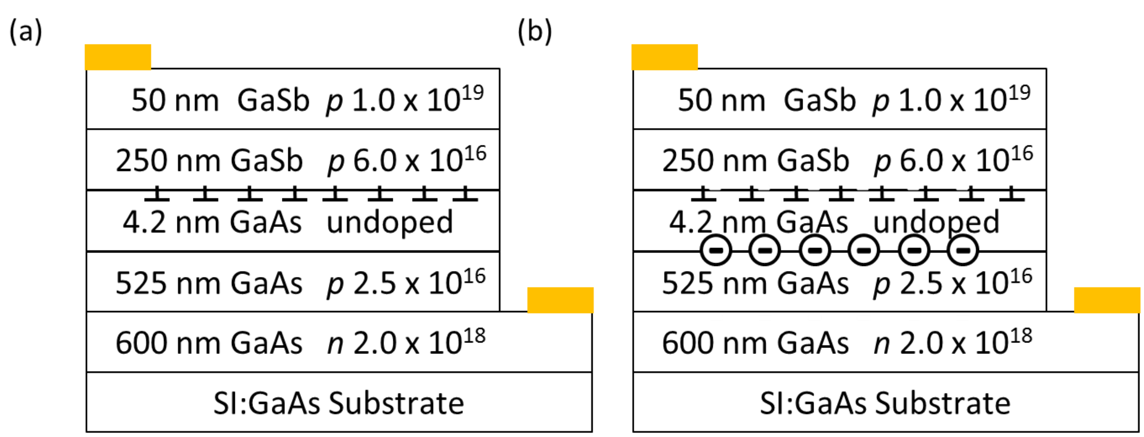

Figure 29: (a) Uncompensated device. (b) Delta-doped device. Two delta-doped devices were grown: a "lightly" doped version with 3.75 x 10^{11} cm^{-2} sheet charge and a "heavily" doped version with 7.50 x 10^{11} cm^{-2} sheet charge.

3. Fabrication

The samples are grown using a solid source molecular beam epitaxy reactor using cracked As and Sb sources (As_2 and Sb_2). The growth conditions include standard substrate temperatures (580°C for GaAs and 510°C for GaSb), V/III ratios (10 for GaAs and 4.4 for GaSb), and growth rates of 0.4 µm/hour. Growth details surrounding the interfacial misfit array can be found elsewhere.[18] An *n*-type delta-doped region is placed 4.2 nm from the IMF interface. This distance places the interface charge at the IMF within a Debye length of the IMF to shield the acceptor charge.[21] Three structures are grown: an uncompensated IMF, a lightly delta-doped (3.75×10^{11} cm^{-2}) IMF, and a heavily delta-doped ($7.5 \times 10^{11} cm^{-2}$) IMF. Silicon is used as an n-dopant for the GaAs and delta-doping. The delta-doping is achieved by closing the gallium shutter and maintaining a constant As flux while opening the Si shutter. The overall growth interruption was 2.6 minutes for the lightly delta-doped and 5.2 minutes for the heavily delta-doped samples. The Si cell temperature is the same for both delta-doped samples, and the delta-doping time was minimized to eliminate the possibility of contamination. The uncompensated sample does not have a growth interruption. Beryllium is used as the p-dopant for the GaSb contact layer. The 250 nm GaSb region above the IMF is unintentionally doped, but has an intrinsic acceptor concentration of approximately $6 \times 10^{16} cm^{-3}$, based upon room temperature Hall calibrations and *C-V* data. After growth, the wafer is cleaved and fabricated into mesas of various sizes using standard photolithography. The samples are etched using an inductively coupled plasma of BCl_3 and Ar and are neither passivated nor dipped in acid to remove dry etching contamination. Contacts are deposited using e-beam evaporation, with Ti/Pt/Au contacts to p-GaSb and Ge/Ni/Ge/Au contacts to n-GaAs. The n-GaAs metal stack requires rapid thermal annealing for 30 seconds at 360°C to form an ohmic contact. The contact is verified to be ohmic using TLM measurements, and has a contact resistance less than 5×10^{-4} Ω cm^2.

4. *I-V* vs. Temperature Measurements & Activation Energies

The J-V curves for all three samples at 300 K are found in Figure 1(b) for a 200 µm diameter mesa. There is a significant difference between the reverse leakage current at all biases, as well as changes in the overall shape of the curves. Both delta-doped samples exhibit three regimes: (i) a low-leakage regime at low bias; (ii) a rapid increase in leakage current between 1-4 V reverse bias; and (iii) a slowly increasing regime at higher reverse bias. These regimes are interpreted as (i) where the GaAs is being depleted, (ii) where the IMF interface charge is depleted, and finally (iii) where the GaSb is depleted. The change from (i) to (ii) takes place at -1.9 V and -0.9 V for the lightly and heavily delta-doped samples, respectively. The overall leakage current densities are at or below the expected values for a homoepitaxial GaSb-based junction.[22] The uncompensated IMF sample has a very low leakage throughout the biases shown, as expected from a high bandgap GaAs *p-n+* junction. However, a breakdown field is reached at -17.5 V, and the leakage current increases exponentially. The samples display a large variation in ideality factor, η, and possible interpretations include both space-charge limited current or the formation of a system of junctions.[23,24] The low series resistance (<50 Ω), existence of a delta-doped heterojunction in series with the *p-n+* junction, lack of an insulating region, and multiple logarithmic slopes in forward bias imply that a system of junctions is the correct interpretation.

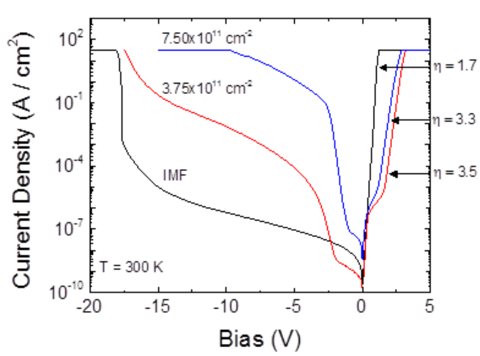

Figure 30: Room temperature *I-V* across samples for 200 µm mesa diameter

J-V plots of each sample against different mesa sizes at 300 K are given in Figure 31. The plots indicate a minor surface component to the leakage, depending on how quickly the IMF is depleted. The uncompensated IMF sample shows the broadest voltage range of surface leakage, with the surface component disappearing around -15 V. The two delta-doped samples exhibit surface-limited leakage currents until -1.7 V and -0.9 V for lightly and heavily delta-doped samples, respectively. These values correspond well to the rapid increase in leakage, and provide further evidence that the surface current is originating in the GaAs. The surface component for all samples disappears almost entirely below 200 K (not shown). This result is unexpected, as GaSb is generally considered to have a very unstable surface prone to leakage, whereas GaAs is much more stable.[25]

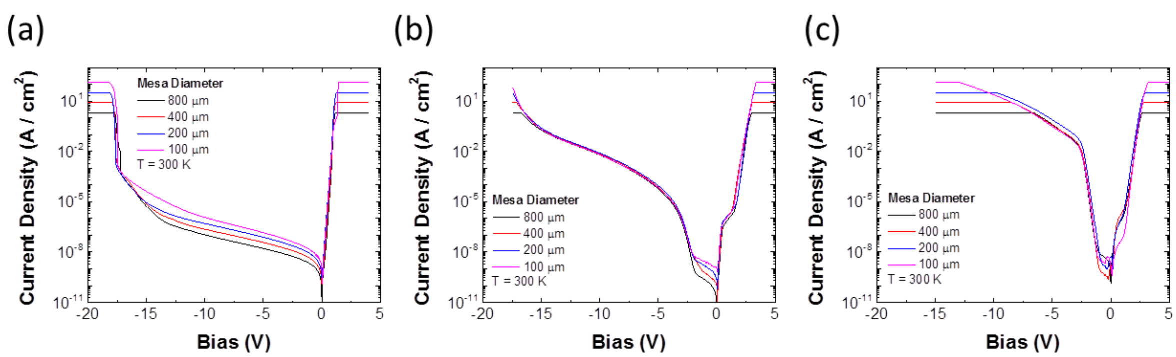

Figure 31: *I-V* curves for all three samples at room temperature across mesa diameter: (a) uncompensated sample (b) lightly delta-doped sample (c) heavily delta-doped sample.

5. *C-V* vs. Temperature Measurements

C-V measurements of the samples at 300 K are found in Figure 32(a) for a 200 μm diameter mesa and at 1 MHz signal frequency. All C-V measurements were terminated once the phase angle increased beyond -80°, ensuring accurate capacitance values. The calculated capacitance for the GaAs junction is included as a guide to the eye, as is the calculated capacitance for a GaSb/GaAs junction based on the sample structure for an uncompensated IMF without interface charge or a conduction band offset. The measured uncompensated IMF sample begins with a standard GaAs diode fall-off before depletion halts at -2 V, closely matching the calculated capacitance. At larger reverse biases, the calculated value drops substantially, and the difference between the measured data and the calculated model indicates that charge redistribution has taken place. From the IMF interface to near breakdown (-15 V) there is only a slight change in the overall depletion, confirming that the interfacial charge is heavily p-type and that the diode barely depletes into the GaSb. The delta-doped samples exhibit a similar trend, albeit with changes at much lower reverse biases and the delta-doping depleting the p-GaAs at zero bias. The curves demonstrate the substantial effect of the interface charge, carrier redistribution, and delta-doping on depletion.

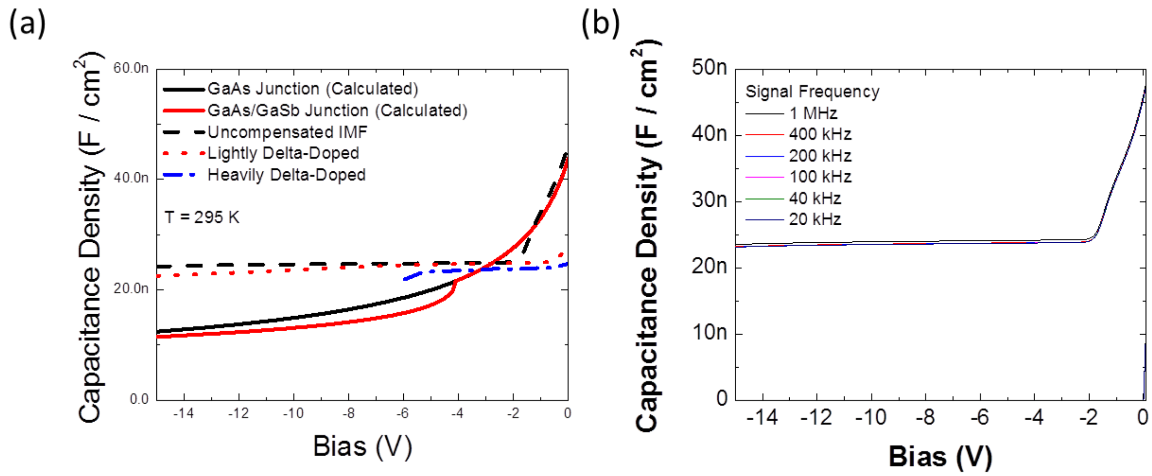

Figure 32: (a) C-V curves of measured and modeled structures. (b) C-V curves across different frequencies for the uncompensated device.

The relationship between signal frequency and measured capacitance is given in Figure 32 (b) for an uncompensated IMF sample. These measurements are performed to exclude the possibility of surface state effects on measured capacitance. The uncompensated IMF, which has the greatest degree of surface leakage, exhibits identical C-V behavior from 20kHz - 1MHz. The capacitance density also scales with area for all three samples.

The doping concentration is calculated using a standard $1/C^2$ fit for a one-sided junction and plotted for all three samples in Figure 33 (a). The measured acceptor doping concentration in the GaAs is 2.8×10^{16} cm^{-3}, which is within the expected error for doping. The calculated depletion width for the uncompensated IMF is 261 nm, and the measured depletion width is 252 nm. Meanwhile, IMF interface is measured at 478 nm from the junction for all three samples, as opposed to 525 nm. This shift is caused by the fixed interface charge at the IMF, which is known to affect the measured depth[26] and is typically recalibrated.[4]

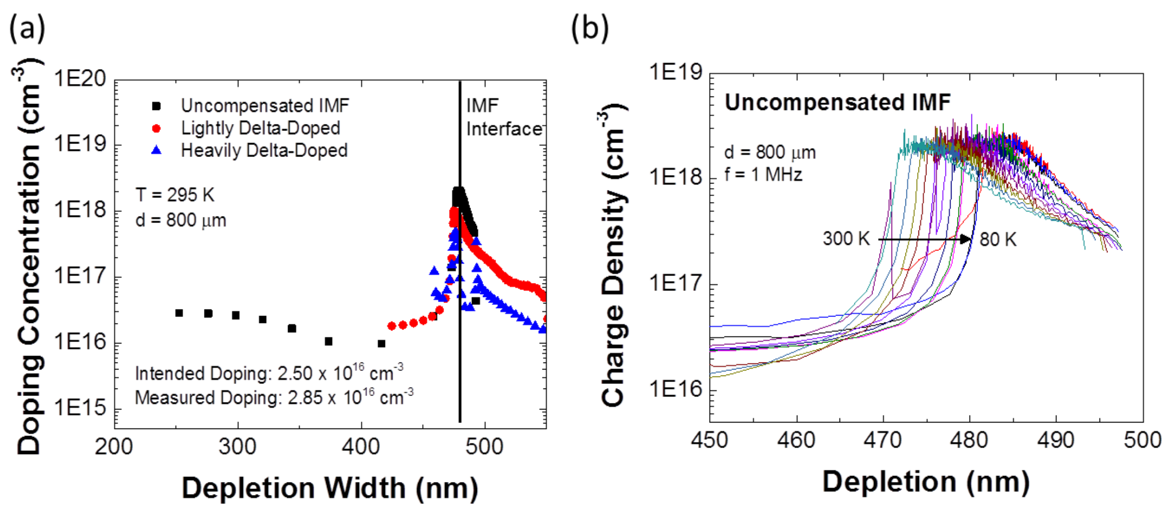

Figure 33: Doping concentration vs. depletion width for all three samples. (b) Temperature dependent measurement for the uncompensated sample.

The charges are integrated against the assumed doping values for both the IMF and lightly delta-doped sample in order to determine the interface charge.[4] The assumed doping concentrations are 2.8 x 10^{16} cm^{-3} for the *p*-GaAs and 6.0 x 10^{16} cm^{-3} for the GaSb. The heavily delta-doped sample was not measured, as the depletion began too close to the IMF region to accurately determine the carrier distribution in the GaAs. The calculated charge density for the uncompensated IMF is (1.80±0.2) x 10^{12} cm^{-2} and the calculated charge density for the lightly delta-doped sample is (1.38±0.1) x 10^{12} cm^{-2}. The errors are based upon assumed uncertainty in the acceptor doping concentration (2.5-3.0 x 10^{16} cm^{-3}), differences across mesa sizes (200, 400 and 800 μm diameters), and differences across signal frequencies (100kHz and 1MHz). There were no trends in the calculated interface charge with mesa size or frequency. The difference between the delta-doped and uncompensated charge densities is 4.28 x 10^{11} cm^{-2}, as compared to the expected 3.75 x 10^{11} cm^{-2} delta-doping concentration. These values are similar in magnitude and represent less than 15% error, providing reassurance that the calculated interface charge is correct. Temperature dependent measurements of the carrier concentration are also performed. As seen in Figure 33 (b), the difference between carrier distributions across temperature is fairly small. This indicates that the interface charge remains relatively constant, and that the interface charge is not driven by a thermally-activated trap-state. The substantial deviation between the Lomer dislocation density (3 x 10^{12} cm^{-2}) and the measured interface charge (1.8 x 10^{12} cm^{-2}) is most likely caused by either the hybridization of the gallium dangling bonds or the introduction of donor-like interface charges from a band discontinuity.

6. Activation Energies

The capacitance data can also be used to generate activation energies for majority carrier states generated in the IMF region via admittance spectroscopy. The ability to control the depletion volume allows for careful consideration of the location of trap-states and band offsets. The changes in G / ω based upon frequency for an uncompensated IMF at -1 V are shown in Figure 34 (a). The clear shift in the peak location with temperature signifies charge trapping. However, further depletion of the junction reduces the intensity of the signal, and -1.5 V is the last remaining bias at which an accurate fitting can take place, as seen in Figure 34 (b). Since the G / ω curves are not perfectly Gaussian, each curve is fit using a two-peak fitting algorithm. The low temperature peak is denoted as “Peak A”, while the higher temperature peak is labeled “Peak B”. The activation energy of the state is then calculated to determine the energy, as seen in Figure 34 (c) and (d).[27] The emission is assumed to be thermionic, implying an emission equation of the following form: $e_n \propto T^2 e^{qE_A / k_B T}$.[28] Both Peak A and Peak B have similar activation energies – inferring the same state is producing a non-Gaussian response – and show a similar bias dependence. The bias dependence and multi-Gaussian fitting is caused by the GaSb/GaAs valence band offset. This result is similar to those seen in $Si/Si_{1-x}Ge_x$ heterostructures and GaSb/GaAs quantum dots.[9,28] Neither delta-doped sample provided a response, indicating that the enhanced fields created at the interface by delta-doping allow carriers to tunnel more efficiently, or minimize the effect of the barrier.

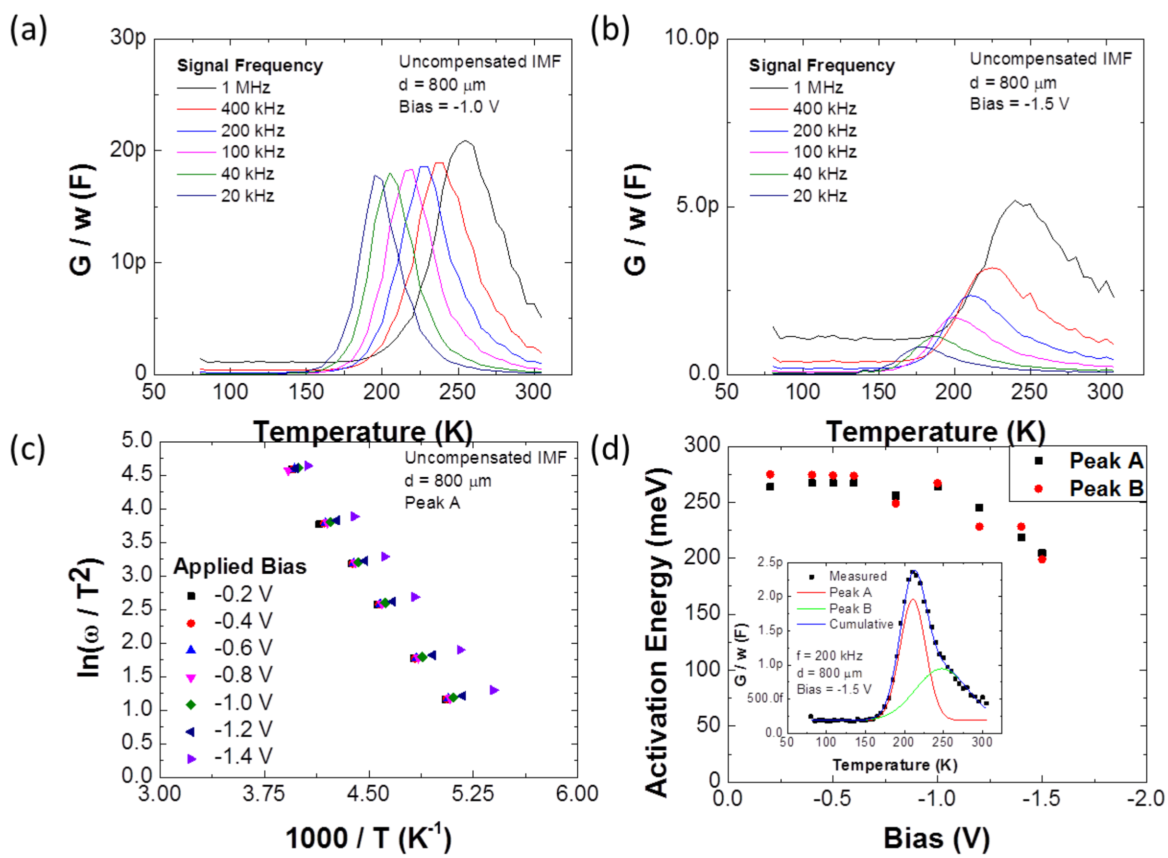

Figure 34: (a) Admittance spectroscopy of uncompensated sample at -1.0 V. (b) Admittance spectroscopy of uncompensated sample at -1.5 V. (c) Arrhenius plot for thermionic emission of various bias voltages. (d) Activation energy vs. bias based on Arrhenius plot, and inset shows fitting for Peak A and Peak B.

Further probing of the interface is accomplished using *J-V* against temperature. The temperature dependent *J-V* for the three structures is found in Figure 35 (a-c). The uncompensated IMF and lightly delta-doped samples display evidence of avalanche behavior at approximately 14-18 V reverse bias, where the dark current increases substantially. This is verified by the decrease in the breakdown voltage with decreasing temperature, which is generally indicative of an avalanche process instead of tunneling. The breakdown voltage also indicates that *p*-GaAs region has been fully depleted and is almost exactly that predicted by dead-space multiplication theory in GaAs for a 525 nm multiplication region (-17.5 V).[29] The lightly delta-doped sample shows a similar trend, but requires significantly more GaSb depletion before reaching the correct field strength. However, breakdown occurs much sooner in the lightly delta-doped sample, indicating that the width of the GaAs multiplication region is considerably smaller, or that the fields are higher. The heavily delta-doped sample does not experience breakdown, implying weaker electric fields and faster depletion through the interface.

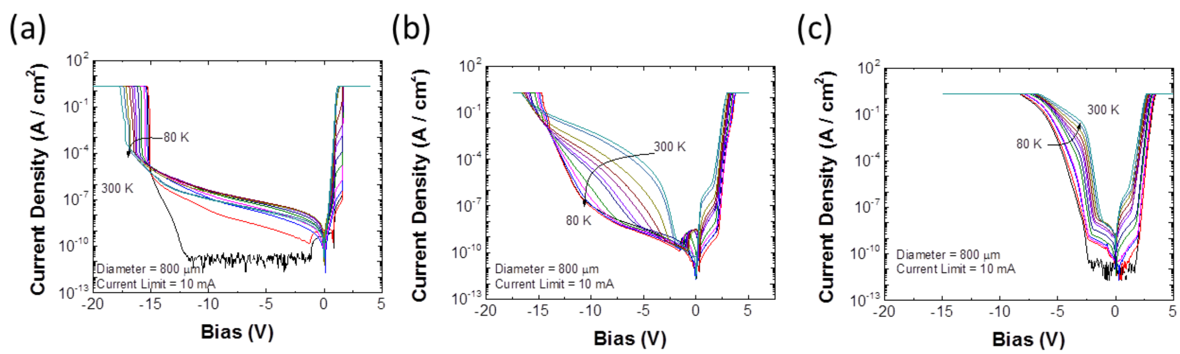

Figure 35: Temperature dependent *J-V* for (a) uncompensated, (b) lightly-delta-doped, and (c) heavily delta-doped samples.

The temperature dependence of the leakage currents also changes dramatically. The uncompensated IMF sample exhibits little change in the overall leakage with temperature (<10^2 times), indicating a very high activation whereas the two delta-doped samples exhibit large changes in leakage (10^5 to 10^7 times) across the temperature range. A semilog plot of the leakage current against inverse temperature gives some indication of the barrier encountered by the minority carriers.[30] In order to decouple surface effects from bulk effects, only biases above the bulk-limited leakage currents are used. An example for a lightly delta-doped sample is given in Figure 36 (a), and the activation energy is fit to an Arrhenius relation, e.g. $\exp(-qE_A/kBT)$. The fit is performed to the high temperature region only, as the low temperature region is measurement limited and/or contains non-classical transport, e.g. avalanching. Errors are calculated based on several diodes of different sizes, and compiled in Figure 36 (b). Both lightly and heavily delta-doped samples show bias-dependent activation energies, indicating that field-dependent tunneling is taking place. The lightly doped sample also shows minimal change until -4 V, and appears to be pinned at 710 meV for low reverse bias. This activation energy corresponds to the approximate difference between the GaAs and GaSb conduction bands at the given doping levels. Also of note is that when the activation energies of the lightly and heavily doped samples are the same, the leakage currents are within an order of magnitude. For instance, given measured activation energies of 500 meV, the heavily delta-doped sample has a leakage current of 0.84 mA and the lightly delta-doped sample has a leakage current of 0.083 mA. This indicates that the barrier height dictates leakage from the GaSb bulk region.

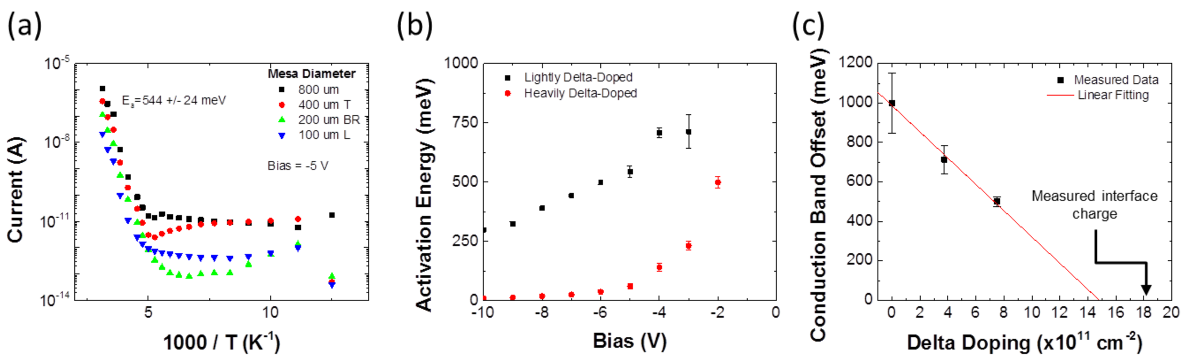

Figure 36: (a) Arrhenius plot of dark current for lightly delta-doped sample. (b) $E_A$vs. bias for both lightly and heavily delta-doped samples. (c) Plot of energy offsets between *n+* GaAs conduction band and samples.

The activation energies from J-V versus temperature are combined with the activation energy from admittance spectroscopy to show the effective conduction band offsets, or barrier, for all three samples in Figure 36 (c). The error for the admittance spectroscopy is based on uncertainty regarding Fermi level location relative to the valence band in GaAs, as the location of the Fermi level in a semiconductor must be known *a priori* in order to accurately calculate band offsets in semiconductors.[8] The midpoint is the nominal E_{Fermi} position 153 meV above the valence band. The slope is relatively linear and the intercept between zero effective conduction band offset and delta doping is 1.48 x 10^{12} cm^{-2}, or within 20% of the expected interface carrier density of 1.8 x 10^{12} cm^{-2}. The minimal conduction band offset has been calculated previously through several *ab initio* calculations.[31]

7. Discussion

The results of this study will hopefully lead to more accurate modeling of structures seeking to pass current through a GaSb/GaAs IMF, particularly photodiodes. However, the large measured conduction band offsets are a concern. These offsets have the potential to severely limit the collection efficiency of photo-generated carriers in the GaSb, and previous reports of *p*-GaSb/*n*-GaAs heterojunctions have indeed shown large effective conduction band offsets (>300 meV) that limited the GaSb photoresponse.[32] The higher offsets measured here are most likely a result of the heterostructure (*p*-GaSb/*p*-GaAs), and our results could suggest a Type-II structure, with holes confined in the GaAs and electrons confined in the GaSb. We do not believe that to be the case. Instead, given the similar separation between E_F and E_{VB} in both the GaAs and GaSb, we believe that Fermi-level pinning at least 300 meV below the GaAs valence band is necessary to explain the measured offsets. In fact, studies using first principles modeling[33] and photoelectron spectroscopy[34] predict or experimentally measure an Sb-induced state 400-500 meV below the valence band maximum of GaAs in Sb-reconstructed surfaces. These values are in keeping with our result, and indicate that delta-doping can be utilized to control the effective band offsets, much like lattice-matched doping interface dipoles.[35]

8. Conclusion

The interface charge density at a GaSb/GaAs IMF was measured using the C-V profiling technique. The results indicate that interface charge is substantial, yet lower than previous *ab initio* calculations. Delta-doping is shown to control depletion through the interface, and changes the effective conduction band offset between the GaSb and GaAs. The optimum amount of delta-doping remains an open question, as a minority carrier barrier between the low-bandgap GaSb and higher bandgap GaAs should offer a trade-off between leakage and GaSb photoresponse. The results are also promising for avalanche photodiode operation, which is pursued further in the next chapter.

9. References

1 A. Rizzi and H. Lüth, Applied Physics A: Materials Science & Processing **75** (1), 69 (2002).

2 D. Arnold, A. Ketterson, T. Henderson, J. Klem, and H. Morkoc, Journal of Applied Physics **57** (8), 2880 (1985).

3 R. Dingle, H. L. Stormer, A. C. Gossard, and W. Wiegmann, Applied Physics Letters **33** (7), 665 (1978).

4 H. Kroemer, Wu-Yi Chien, Jr J. S. Harris, and D. D. Edwall, Applied Physics Letters **36** (4), 295 (1980).

5 D. V. Lang, Journal of Applied Physics **45** (7), 3023 (1974).

6 D. L. Losee, Applied Physics Letters **21** (2), 54 (1972).

7 C. Cai, M. I. Nathan, and T. H. Lim, Applied Physics Letters **74** (5), 720 (1999).

8 D. V. Lang, M. B. Panish, F. Capasso, J. Allam, R. A. Hamm, A. M. Sergent, and W. T. Tsang, Applied Physics Letters **50** (12), 736 (1987).

9 K. Nauka, T. I. Kamins, J. E. Turner, C. A. King, J. L. Hoyt, and J. F. Gibbons, Applied Physics Letters **60** (2), 195 (1992).

10 T. Won, G. Munns, R. Houdre, and H. Morkoc, Applied Physics Letters **49** (19), 1257 (1986).

11 Yi Wang, P. Ruterana, S. Kret, J. Chen, S. El Kazzi, L. Desplanque, and X. Wallart, Applied Physics Letters **100** (26), 262110 (2012).

12 Li Yang, Mayank T. Bulsara, Kenneth E. Lee, and Eugene A. Fitzgerald, Journal of Crystal Growth **324** (1), 103 (2011).

13 G. Balakrishnan, S. Huang, L. R. Dawson, Y. C. Xin, P. Conlin, and D. L. Huffaker, Applied Physics Letters **86** (3), 034105 (2005).

14 W. E. Hoke, R. E. Leoni, C. S. Whelan, T. D. Kennedy, A. Torabi, P. F. Marsh, Y. Zhang, C. Xu, and K. C. Hsieh, Journal of Vacuum Science & Technology B: Microelectronics and Nanometer Structures **22** (3), 1554 (2004).

15 S. Mendach, C. M. Hu, Ch Heyn, S. Schnüll, H. P. Oepen, R. Anton, and W. Hansen, Physica E: Low-dimensional Systems and Nanostructures **13** (2–4), 1204 (2002).

16 Farseem Mohammedy and M. Jamal Deen, Journal of Materials Science: Materials in Electronics **20** (11), 1039 (2009).

17 W. K. Liu, D. Lubyshev, J. M. Fastenau, Y. Wu, M. T. Bulsara, E. A. Fitzgerald, M. Urteaga, W. Ha, J. Bergman, B. Brar, W. E. Hoke, J. R. LaRoche, K. J. Herrick, T. E. Kazior, D. Clark, D. Smith, R. F. Thompson, C. Drazek, and N. Daval, Journal of Crystal Growth **311** (7), 1979 (2009).

18 S. H. Huang, G. Balakrishnan, A. Khoshakhlagh, A. Jallipalli, L. R. Dawson, and D. L. Huffaker, Applied Physics Letters **88** (13), 131911 (2006).

19 Y. Wang, P. Ruterana, J. Chen, L. Desplanque, S. El Kazzi, and X. Wallart, Journal of Physics: Condensed Matter **24** (33), 335802 (2012).

20 A. Jallipalli, K. Nunna, M. N. Kutty, G. Balakrishnan, L. R. Dawson, and D. L. Huffaker, Applied Physics Letters **95** (20), 202107 (2009).

21 E. F. Schubert, Journal of Vacuum Science & Technology A: Vacuum, Surfaces, and Films **8** (3), 2980 (1990).

22 A. Y. Polyakov, M. Stam, A. G. Milnes, and T. E. Schlesinger, Materials Science and Engineering: B **12** (4), 337 (1992).

23 Murray A. Lampert and A. Rose, Physical Review **121** (1), 26 (1961).

24 Jay M. Shah, Y. L. Li, Th Gessmann, and E. F. Schubert, Journal of Applied Physics **94** (4), 2627 (2003).

25 Z. Y. Liu, T. F. Kuech, and D. A. Saulys, Applied Physics Letters **83** (13), 2587 (2003).

[26] D. C. Look, C. E. Stutz, and K. R. Evans, Applied Physics Letters **56** (7), 668 (1990).
[27] D. L. Losee, Journal of Applied Physics **46** (5), 2204 (1975).
[28] M. Geller, C. Kapteyn, L. Müller-Kirsch, R. Heitz, and D. Bimberg, physica status solidi (b) **238** (2), 258 (2003).
[29] Mohammad A. Saleh, Majeed M. Hayat, Oh-Hyun Kwon, Archie L. Holmes, Joe C. Campbell, Bahaa E. A. Saleh, and Malvin C. Teich, Applied Physics Letters **79** (24), 4037 (2001).
[30] Ker Pin Jern, A. R. J. Marshall, A. B. Krysa, J. P. R. David, and Tan Chee Hing, Quantum Electronics, IEEE Journal of **47** (8), 1123 (2011).
[31] Chris G. Van de Walle and J. Neugebauer, Nature **423** (6940), 626 (2003).
[32] J. Toušková, D. Kindl, E. Samochin, J. Toušek, E. Hulicius, J. Pangrác, T. Šimeček, and Z. Výborný, Solar Energy Materials and Solar Cells **76** (2), 135 (2003).
[33] W. G. Schmidt and F. Bechstedt, Physical Review B **55** (19), 13051 (1997).
[34] P. Laukkanen, R. E. Perälä, R. L. Vaara, I. J. Väyrynen, M. Kuzmin, and J. Sadowski, Physical Review B **69** (20), 205323 (2004).
[35] Federico Capasso, Alfred Y. Cho, Khalid Mohammed, and Philip W. Foy, Applied Physics Letters **46** (7), 664 (1985).

Chapter 6: Characterization of IMF-based Avalanche Photodiodes

1. Background

The final component to any mature photodiode material system is a low noise multiplication material for avalanche photodiode (APD) operation. Silicon, GaAs/AlGaAs, and InP/InAlAs all feature stable, low noise multiplication materials that can be utilized to create gain and improve SNR prior to amplification in the read-out circuitry. Unfortunately, the Antimonides do not have such a multiplication region. While initial research into the AlGaSb material system promised resonant impact ionization from holes in the split-off band,[1] subsequent works found alternative explanations that were more reasonable.[2] Furthermore, all AlGaSb based devices exhibited much higher impact ionization rates for holes than for electrons. Since a hole's mobility and saturation velocity are considerably lower than an electron's, this material system places constraints on the gain-bandwidth product of the APD.[3] Following this point, Marshall et al. demonstrated that it was possible to use electron-only multiplication in an InAs photodiode on an InAs substrate.[4] While these results were promising, InAs has a low bandgap that promotes direct band-to-band tunneling, and therefore large junction widths are necessary in order to produce high gain. An improved design was introduced by Maddox et al., who were able to limit the background doping concentration.[5] Unfortunately, the large depletion width (>5 μm) and high leakage currents (10^{-1} A/cm^2) only proved that InAs could not be used for high performance APDs above 6 GHz.[6] A different solution is needed.

The best option for avalanche gain lies in the Arsenides, and is generally considered to be $Al_{0.8}Ga_{0.2}As$. While the material provides impact ionization to both electrons and holes, the gain for electrons is approximately 10x higher than that of holes. The electron dominated multiplication ensures faster transit times and bandwidths. The material also has very high bandgap (2.01 eV) that precludes the possibility of band-to-band tunneling, even in extremely narrow multiplication regions (<250 nm).

Unfortunately, Arsenide materials have limited lattice-matched bulk bandgaps available to them, and the cut-off wavelength is approximately 870 nm at room temperature. The chosen material system for the 1.55 µm telecommunications industry is InAlAs/InP, which has limited gain-bandwidth product (GBP) as a result of its lower bandgap (1.4 eV). The GBP is generally less than 500 GHz, as shown in Figure 37 (a). Meanwhile, the expected GBP for a 50 nm $Al_{0.8}Ga_{0.2}As$ multiplication region is 500 – 800 GHz, as shown in Figure 37 (b). These values are close to the record GBPs exhibited by Ge/Si and HgCdTe.[7,8] Furthermore, the unity gain bandwidths of the AlGaAs design (essentially the *RC*-limited or transit-limited response times) are much greater than those measured in other systems (< 15 GHz).

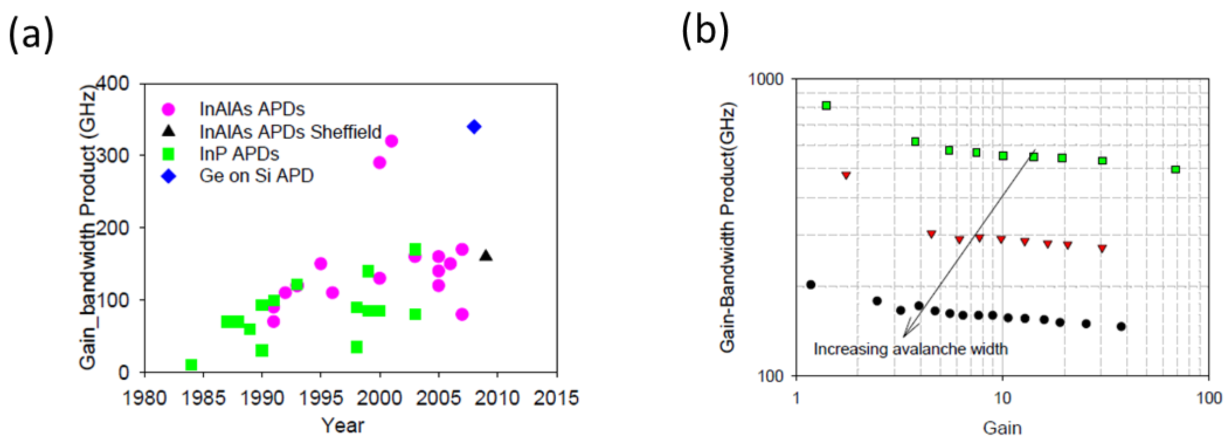

Figure 37: (a) Gain-bandwidth products of various APDs by year. (b) Gain-bandwidth product of $Al_{0.8}Ga_{0.2}As$ APDs with multiplication widths of 50, 100, and 200 nm. Both figures from Tan.[9]

The integration of an Arsenide multiplication region and an Antimonide absorber is possible using the IMF. The interface charge density study in Chapter 5 had the added benefit of demonstrating avalanche breakdown in a GaAs device, indicating that it would be possible to create photodiodes. The temperature dependent measurements also indicated that while there was a barrier between the GaSb and the GaAs, the barrier was surmountable and could be somewhat controlled using delta-doping. The substitution of the GaAs multiplication region for an $Al_{0.8}Ga_{0.2}As$ multiplication region would create the possibility of not only high GBPs, but a hybrid material system with bandgaps from 0.860 to 4.4 µm.

2. Device Design and Fabrication

The initial photodiode design features a thin $Al_{0.8}Ga_{0.2}As$ multiplication region, which lowers both dark current and excess noise. The design was varied across three different devices, each changing the thickness of the *p*-AlGaAs charge sheet to affect depletion through the IMF: a 30 nm charge sheet, a 50 nm charge sheet, and a 65 nm charge sheet. The avalanche region was designed to be only 50 nm wide in order to facilitate dead space effects in the multiplication and reduce the overall transit time of the carriers.[10] A 40 nm undoped GaAs region was also placed between the IMF and the charge sheet in order to facilitate proper IMF formation and allow the electrons to regain energy after passing through the IMF barrier. The samples were processed using standard photolithography, etching, and contact metallization. The only difference between these samples and previously discussed samples was the lack of an HCl clean-up dip after dry etching.

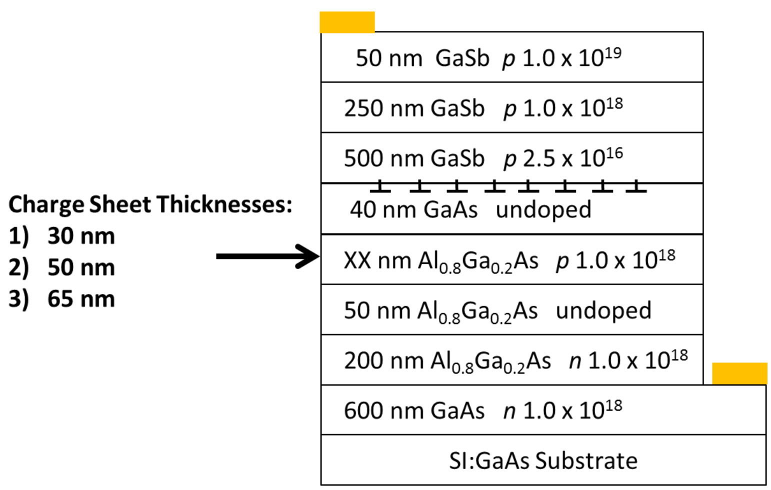

Figure 38: (a) GaAs-based multiplication design (b) $Al_{0.8}Ga_{0.2}As$-based multiplication design.

3. $Al_{0.8}Ga_{0.2}As$ Design *I-V* and Responsitivity

The devices were measured for their dark current characteristics after fabrication. The dark current can be found in Figure 39 (a). The devices exhibit extremely low leakage levels, even at room temperature for 400 µm diameter mesas. (The high bandwidth diodes measured previously were only 20 -50 µm.) Both the 50 nm and 65 nm diodes have overall reverse leakage values less than 100 pA over the range from 0 to -8 V, and show breakdown at -11 V. Meanwhile, the sample with a 30 nm charge sheet has two distinct regions. The first region is an exponential increase in the reverse leakage current from -2 V to -8 V, followed by a slower trend from -8 V until the onset of series resistance at -11 V. All three diodes exhibit low series resistance (<100 Ω) and ideality factors of approximately 1.9. The devices are subsequently illuminated using 1.55 µm laser, and the results are shown in Figure 39 (b). Similar trends to the dark current are evident, and the photocurrent clearly increases per unit bias with decreasing charge sheet thickness. However, a substantial increase in the photocurrent for the 30 nm charge sheet indicates that the IMF barrier is lowered more effectively. Unfortunately, no clear avalanching effect is visible in the 30 nm charge sheet device, whereas the 50 nm and 65 nm devices experience breakdown in the photocurrent at -11 V.

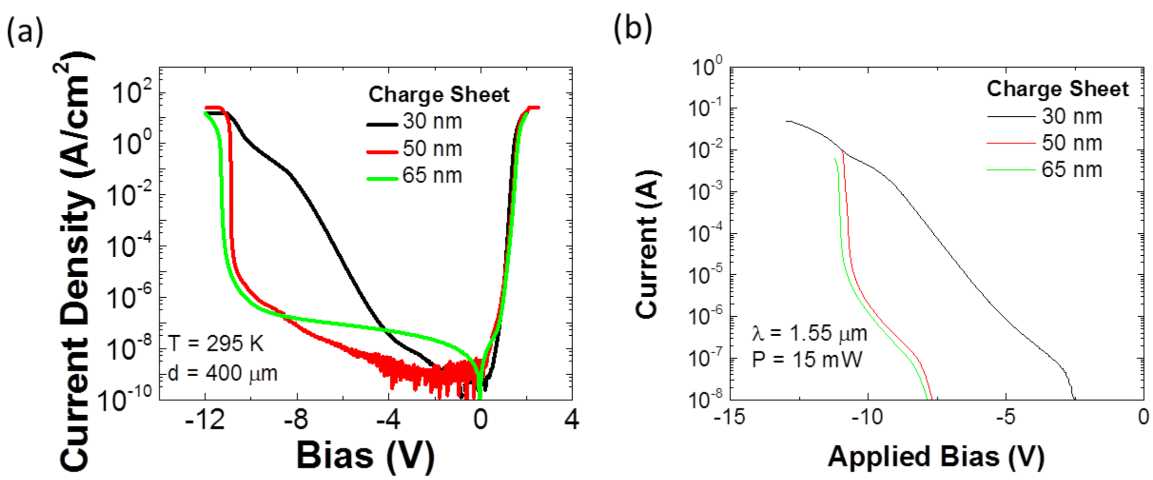

Figure 39: (a) Dark I-V of three $Al_{0.8}Ga_{0.2}As$ designs. (b) Photocurrent of all three designs for 15 mW, 1.55 µm laser.

4. $Al_{0.8}Ga_{0.2}As$ Design *C-V* Measurements and *I-V* vs. Temperature

The *I-V* and photoresponse measurements indicate that the IMF acts as a barrier to the photocurrent, as expected from the interface charge study. However, more evidence is needed to prove the IMF is being depleted, and that the 30 nm sample is indeed avalanching. A set of *C-V* measurements to measure the depletion are shown in Figure 40 (a). The 50 nm and 65 nm devices appear very similar in all portions of the *C-V* curve. The *C-V* curves can be divided into three regions: (i) from 0 V to -2 V, the nominally undoped GaAs region is depleted, as are any interfacial charges from the GaAs/AlGaAs heterojunction; (ii) from -2 V to -6 V, the AlGaAs charge sheet is being depleted; and (iii) from -6 V to -10 V, the IMF starts to be depleted. The very small change in capacitance from -6 V to -10 V is analogous to the *C-V* curve in the interface charge study, and builds substantial field (approximately -11 V) across the 140 – 155 nm space charge region. The average field over this region is over 500 kV/cm near breakdown, which provides large gains.[11] Meanwhile, the 30 nm device appears to be greatly depleted from zero bias, as it has lower capacitance over almost the entire voltage range. It is also able to deplete the IMF much more rapidly, as seen by the tail from -7 V to -8 V. The existence of impact ionization is verified using temperature dependent measurement of *I-V*, as shown in Figure 40 (b). The leakage current is extremely low throughout the entire temperature range, but at -10 V the lower temperatures exhibit higher leakage. Even with the large amount of depletion through the IMF, the device still operates as an APD.

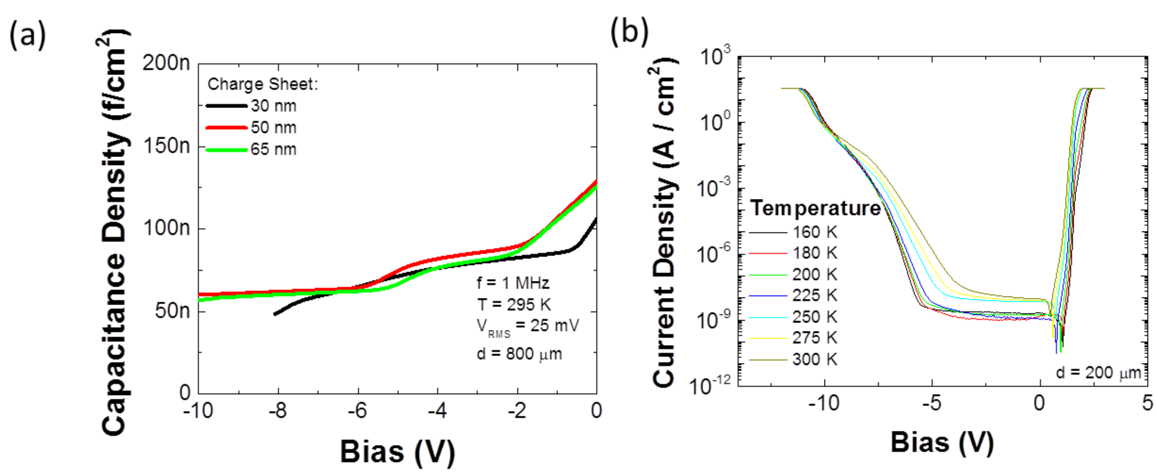

Figure 40: (a) C-V curves for all three devices. (b) Temperature dependent I-V of 30 nm device.

5. Further Enhancements using Delta-Doping

The results from the $Al_{0.8}Ga_{0.2}As$ structures provided two new insights into the feasibility of Arsenide/Antimonide APDs: (1) APDs using IMF-based absorbers were possible and (2) the barrier between the IMF-based GaSb and GaAs blocked a significant percentage of the photogenerated carriers. The most important component appeared to be (2), as carrier collection in AlGaAs/GaAs photodiodes has been addressed previously.[12] The previous study on interface charge density and delta-doping was modified slightly in order to address this issue. The new design increased the GaSb absorber thickness and decreased the delta-doping intervals, as shown in Figure 41. The enhanced devices have a maximum expected photoresponse of 0.43 A/W based on the 750 nm GaSb absorber. The devices were grown and fabricated in the manner described in Chapter 5.

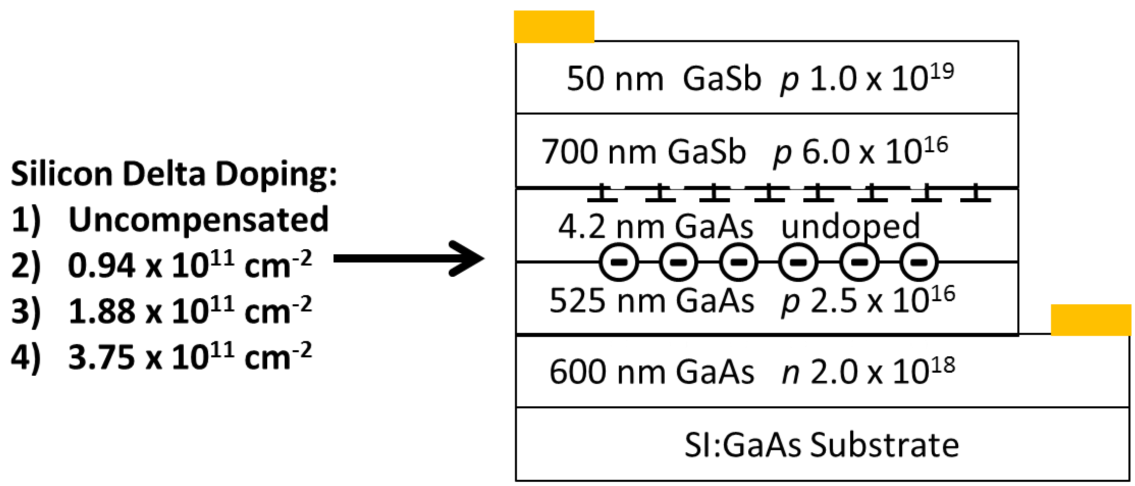

Figure 41: Enhanced APD Design featuring a GaAs multiplication region

6. Temperature-Dependent *I-V* of GaAs Design

The *I-V* characteristics of the enhanced devices were measured to determine the effects of delta-doping on leakage current. The previous results from the interface charge measurements indicated that while the interface charge density at the IMF was only 1.81 x 10^{12} cm^{-2}, only a small amount of delta-doping could prevent the device from avalanching. As seen in Figure 42, the delta-doping was able to completely control the leakage current from the low-bandgap GaSb absorber region. Furthermore, all four enhanced devices exhibited multiplication. The devices were then measured in a cryogenic probestation to verify the existence of avalanche gain. The breakdown voltages against temperature are shown in Figure 42 (b). The temperature coefficient of breakdown voltage is 11.3 mV/K over the linear part of the curve between 100 – 300 K, which matches other values from the literature, but is not as low as AlGaAs.[13]

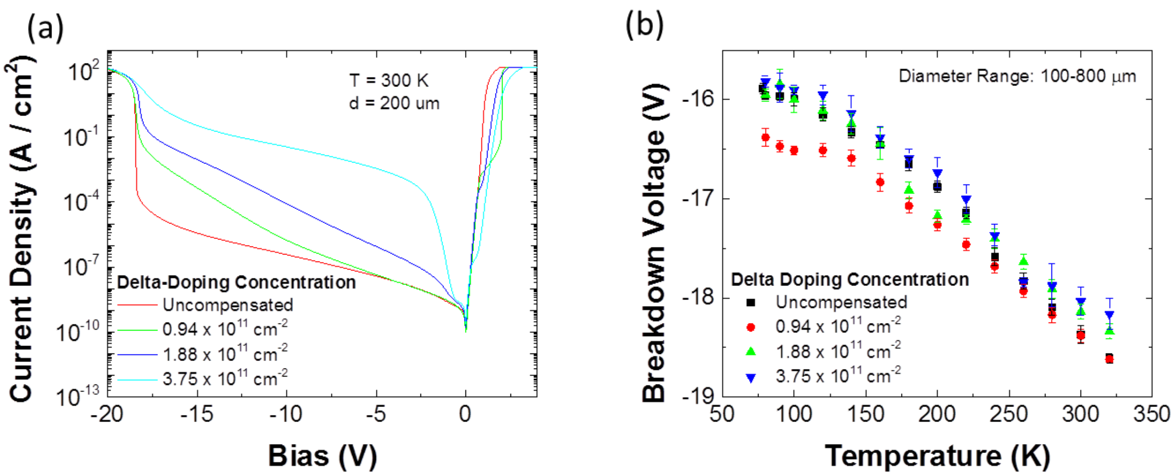

Figure 42: (a) Room temperature *J-V* of various delta-doped samples. (b) Temperature dependence of breakdown for all four delta-doped samples.

The temperature dependent *J-V* curves were measured in order to determine breakdown. The curves can be found in Figure 43. There are several interesting features. The uncompensated sample in Figure 43 (a) shows the same extremely high activation energy that was seen in the interface charge density study. The repeatability of these curves, even with a thicker GaSb absorber, is important. The second point is that the devices appear to find a leakage floor between 10^{-8} to 10^{-9} A/cm^2 at low temperatures. All but the highest delta-doping level exhibits this trend, and it is unclear if the Silicon delta-doping is being frozen out, or if this corresponds to carriers in the GaSb being frozen out. Third, the soft breakdown of the 3.75 x 10^{11} cm^{-2} sample, Figure 43 (d) appears to be a direct result of the series resistance. The extra leakage current of the device creates a higher ohmic loss at the contacts, which prevents the devices from exhibiting the nearly vertical increase in leakage found in the other samples. Finally, it should be noted that the voltage sweep was from positive to negative to prevent premature breakdown in the devices, which would also depend on the mesa diameter (larger mesas, more carriers, more likelihood of initiating an avalanche). Complex junctions such as the one described here are known to possess some forms of hysteresis, and the forward bias characteristics are sweep dependent. However, all devices exhibit the effects of impact ionization, making them strong candidates for APD operation.

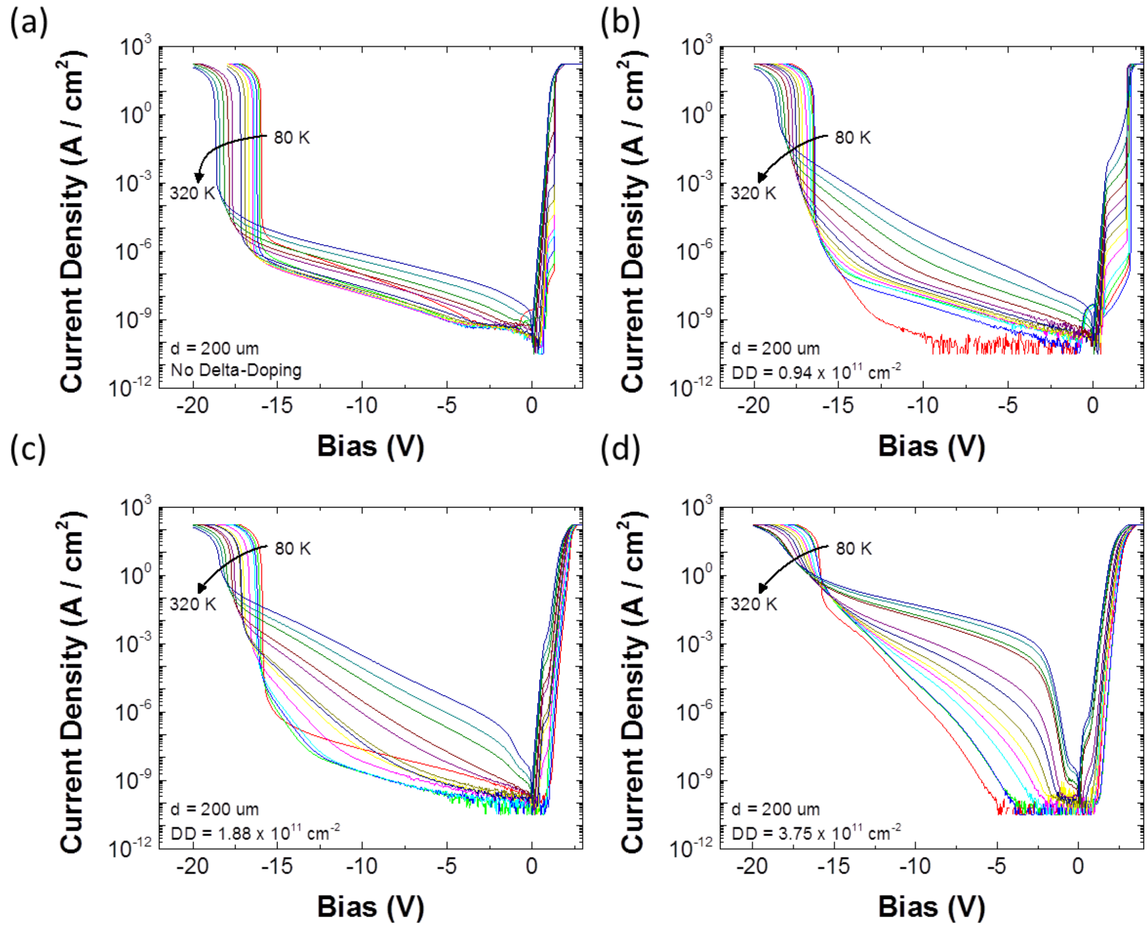

Figure 43: *J-V* vs. temperature for all four enhanced IMF APDs. All temperature steps are by 20 K.

7. Responsivity Measurements of GaAs Design

The photodiode responsivity measurement was taken at 295 K using a 1.55 μm laser and an optical power of 15 mW. The resulting external quantum efficiency values are shown in Figure 45. The delta-doping is clearly aiding the photoresponse, as could be expected from both the AlGaAs APD study and the calculated conduction band offsets from the interface charge study. Furthermore, each device exhibits multiplication gain in the region of -15 V to -20 V, with smaller amounts of gain for increasing delta doping. However, the delta doping increases the photoresponse dramatically, and photoresponse at 0 V is possible using the 1.88 x 10^{11} cm^{-2} device.

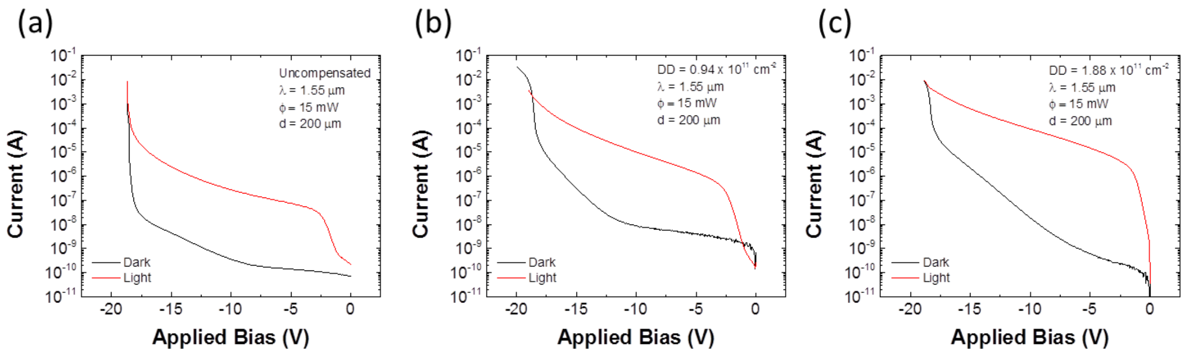

Figure 44: Room temperature photoresponse of APDs with GaAs multiplication regions. The delta doping concentrations are: (a) no delta doping (b) 0.94 x 10^{11} cm^{-2} and (c) 1.88 x 10^{11} cm^{-2}

A more accurate measurement of the effects of delta-doping is the unmultiplied quantum efficiency. That value represents a true indicator of any barrier lowering at the IMF, and does so by dividing out the effects of multiplication. The unmultiplied quantum efficiency of the enhanced devices is shown in Figure 45 (a), and the maximum expected value for a 750 nm GaSb absorber is 35.2%, taking into account only reflection losses and absorption. The unmultiplied quantum efficiency increases by a constant factor of 10 between the 1.88 x 10^{11} cm^{-2} and 0.94 x 10^{11} cm^{-2} samples, and a factor of 100 between the uncompensated and 0.94 x 10^{11} cm^{-2} samples. This represents a 119 meV difference in the effective conduction band offset between the *p*-GaSb and *p*-GaAs for the first 0.94 x 10^{11} cm^{-2} of delta doping samples, and a 59 meV difference for the second, assuming Boltzmann statistics. It is not possible to determine the offset of the IMF based on the expected quantum efficiency, as other considerations for IMF recombination velocity must be made. A plot of the quantum efficiency and dark current are given in Figure 45 (b) at a bias of -10 V. Interestingly, the factor of 100 increase in unmultiplied quantum efficiency corresponds to only a factor of 10 increase in dark current. Meanwhile, the change to even higher delta-doping concentration leads to a factor of 100 increase in dark current for only a factor of 10 increase in photocurrent.

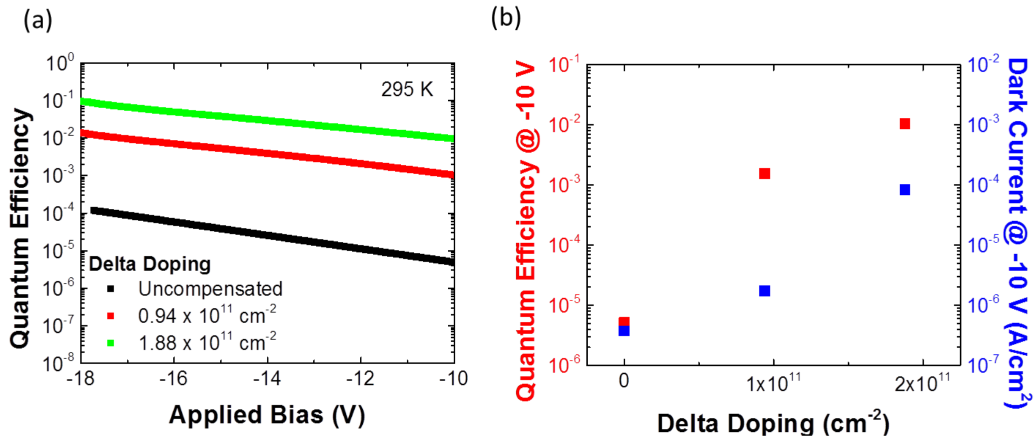

Figure 45: (a) Unmultiplied external quantum efficiency vs. applied bias for three of the delta-doped GaAs APDs (b) Comparison at -10 V of the change in external quantum efficiency and the dark current.

8. Comparison of Responsivity across Designs

For the sake of comparison, a device from the $Al_{0.8}Ga_{0.2}As$ design (50 nm charge sheet) and a device from the GaAs design (200 nm absorber, no delta-doping from interface charge study) were measured for both dark current and responsivity at 1.55 µm. The results can be seen in Figure 46. The AlGaAs device has a much lower dark current than the GaAs device near its breakdown voltage of -11 V, and exhibits three distinct trends in the photoresponse. The photodiode shows no DC photoresponse until -7 V, and then exhibits an exponential rise. Once the bias reaches approximately -8.2 V, the rate slows and the super-exponential multiplication curve appears to dominate the photocurrent. Meanwhile, the GaAs device has an exponential increase in the photocurrent until about -15 V, where the effects of multiplication can be seen. Since the devices are testing two different schemes for electric field confinement in the diode – the AlGaAs device utilizes a standard *p-i-n* structure and the GaAs device uses the IMF as an acceptor sheet to stop depletion – careful attention is paid to the unmultiplied region of the photoresponse. At the onset of multiplication (-8 V for the AlGaAs device and -12 V for the GaAs device), the GaAs device produces approximately the same photocurrent as the AlGaAs device, even though the absorber region is 3.2x thicker in the AlGaAs. The expected responsivity values for both samples are 0.22 A/W in the GaAs device and 0.46 A/W in the AlGaAs device. The low absolute quantum efficiency seen here (microamps) indicates that the IMF acts as a barrier to photogenerated carriers. Furthermore, the similar photocurrents between samples indicates that the use of the interface charge has the additional benefit of reducing the barrier.

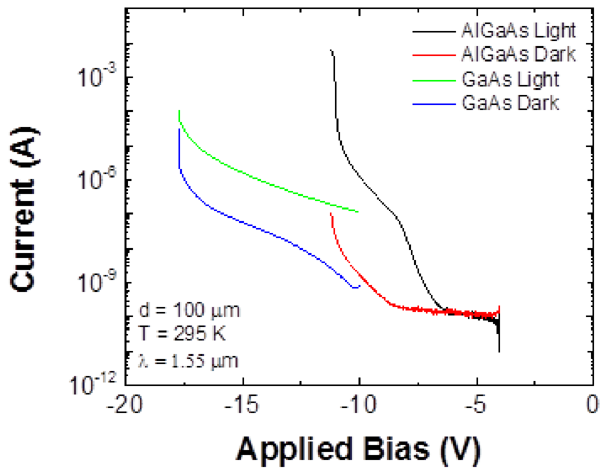

Figure 46: (a) Dark and light curves for AlGaAs and GaAs devices. Only parts of the curve are given for clarity.

9. Excess Noise Measurements

The excess noise values of two device designs were measured in order to determine the effective *k* in comparison to known values from the literature. The excess noise measurement utilized a 1.55 µm laser to avoid the creation of photocurrent in the GaAs and AlGaAs regions, leading to electron-only carrier injection. The samples were connected to a Picosecond 5541A bias-tee, which was in turn connected to an HP 8970B Noise Figure Meter. The noise figure was integrated over 5 MHz bandwidth with a cut-on frequency of 20 MHz. The noise figure meter was also calibrated beforehand using a manufacturer's reference. Multiplication in the device was varied by applying bias across the inductor lead of the bias-tee. The results are shown in Figure 47.

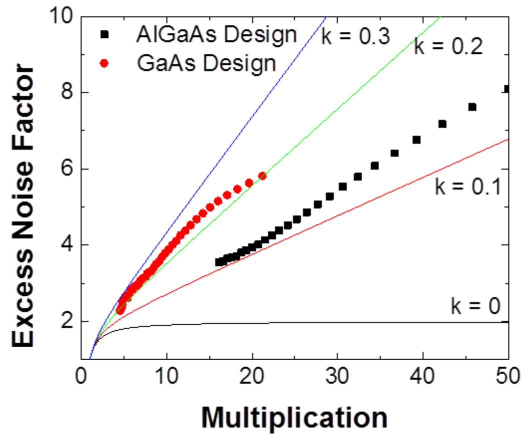

Figure 47: Excess noise characteristics of the uncompensated GaAs design and AlGaAs design with 50 nm charge sheet.

The excess noise characteristics verify that the photodiodes behaved exactly as expected for homojunction devices. The $Al_{0.8}Ga_{0.2}As$ devices feature a very low excess noise factor of 0.1-0.2, and behave identically to previously measured *p-i-n* samples in the literature.[11] The GaAs device has an excess noise that is slightly higher (approximately 0.3) than the AlGaAs device, and appears lower than standard *p-i-n* structures.[14] The most likely explanation for this discrepancy is the higher fields generated near the *p-n+* GaAs junction. The high fields localize the multiplication away from the IMF and closer to the junction itself, giving rise to a dead space effect.[10] A random path length model, which takes into account the fields at all points of the junction, shows a much better degree of matching.

10. Discussion

The results provided here provide a gateway towards extremely high gain-bandwidth products in GaSb-photodiodes. The current record performance for gain-bandwidth in an Antimonide photodiode is 90 GHz, which was set using an $Al_{0.06}Ga_{0.94}Sb$ multiplication region. That device featured a unity-gain cut-off of only 10 GHz, and an effective *k* of 0.2. While this result was impressive, the scope of future improvements was limited. The small bandgap avalanche region (0.7 eV) leads to large tunneling currents at high fields, eliminating the possibility of narrow multiplication regions. Without a narrow multiplication region, it is impossible to engineer dead space effects to lower the excess noise factor. The results shown here do not suffer from either problem. The junction is in a high bandgap region and has a low effective *k*. The avalanche bandwidth limit indicates that the gain bandwidth product of the GaAs devices should be in the range of 100 – 200 GHz, and the AlGaAs devices should have gain bandwidth products between 500 GHz – 1 THz. If these devices are *RC*-limited, they would represent some of the highest gain bandwidth products ever reported. More importantly, they represent a solution to high bandwidth multiplication in the Antimonides.

11. Conclusion

IMF-based avalanche photodiodes utilizing GaSb absorbers and GaAs-based multiplication regions are shown. The $Al_{0.8}Ga_{0.2}As$ design exhibits very low excess noise and dark current, but has low responsivity because of the band offsets. Meanwhile, the GaAs design exhibits high responsivity that can be tuned by the use of delta-doping. The integration of both techniques – an AlGaAs multiplication region that utilizes the IMF as the charge sheet – appears to be the best route to high gain-bandwidth, high sensitivity detectors using the Antimonides as absorbers.

12. References

[1] O. Hildebrand, W. Kuebart, K. Benz, and M. Pilkuhn, Quantum Electronics, IEEE Journal of **17** (2), 284 (1981).

[2] H. Kuwatsuka, T. Mikawa, S. Miura, N. Yasuoka, M. Ito, T. Tanahashi, and O. Wada, Journal of Applied Physics **70** (4), 2169 (1991).

[3] R. B. Emmons, Journal of Applied Physics **38** (9), 3705 (1967).

[4] A. R. J. Marshall, C. H. Tan, M. J. Steer, and J. P. R. David, Applied Physics Letters **93** (11), 111107 (2008).

[5] S. J. Maddox, W. Sun, Z. Lu, H. P. Nair, J. C. Campbell, and S. R. Bank, Applied Physics Letters **101** (15), 151124 (2012).

[6] Andrew R. J. Marshall, Pin Jern Ker, Andrey Krysa, John P. R. David, and Chee Hing Tan, Opt. Express **19** (23), 23341 (2011).

[7] Wissem Sfar Zaoui, Hui-Wen Chen, John E. Bowers, Yimin Kang, Mike Morse, Mario J. Paniccia, Alexandre Pauchard, and Joe C. Campbell, Opt. Express **17** (15), 12641 (2009).

[8] Gwladys Perrais, Johan Rothman, Gerard Destefanis, and Jean-Paul Chamonal, Journal of Electronic Materials **37** (9), 1261 (2008).

9 C. H. Tan, J. S. Ng, S. Xie, and J. P. R. David, presented at the Computers and Devices for Communication, 2009. CODEC 2009. 4th International Conference on, 2009 (unpublished).

10 M. M. Hayat, W. L. Sargeant, and B. E. A. Saleh, Quantum Electronics, IEEE Journal of **28** (5), 1360 (1992).

11 B. K. Ng, J. P. R. David, S. A. Plimmer, G. J. Rees, R. C. Tozer, M. Hopkinson, and G. Hill, Electron Devices, IEEE Transactions on **48** (10), 2198 (2001).

12 Federico Capasso, Alfred Y. Cho, Khalid Mohammed, and Philip W. Foy, Applied Physics Letters **46** (7), 664 (1985).

13 C. Groves, C. N. Harrison, J. P. R. David, and G. J. Rees, Journal of Applied Physics **96** (9), 5017 (2004).

14 K. F. Li, D. S. Ong, J. P. R. David, G. J. Rees, R. C. Tozer, P. N. Robson, and R. Grey, Electron Devices, IEEE Transactions on **45** (10), 2102 (1998).

Chapter 7: Conclusion

This dissertation has demonstrated the possibility of utilizing the structural, optical, and electrical properties of IMF-based GaSb photodiodes for high bandwidth, low noise applications. Key discoveries regarding the correlation factor, bandwidth limitations, interface charge density, barrier offsets, and different avalanche regions have been given. Less favorable discoveries, including low SRH lifetimes, high surface recombination velocities, and Fermi-level pinning at the sidewall, have also been reported. Based on preliminary measurements, an APD with GBP of over 500 GHz should be possible using GaSb absorbers and AlGaAs multiplication regions, with unity gain bandwidths larger than 30 GHz. If the leakage current of these devices can be reduced, this approach presents a path to high performance photodiodes for telecommunications and infrared sensing with cut-offs from 1.7 – 4.4 µm.

1. Five Easy Pieces

Some simple rules for device designers seeking to use the IMF can be established based on the results of this dissertation. First, use a *p*-GaSb top contact and place the *n*-contact at the bottom of the wafer. This approach avoids the infamous *n*-GaSb contact layer. Second, avoid *n*-GaSb if at all possible, as its Fermi level will be pinned at the valence band after etching, leading to a direct shunt path from the *p*-GaSb region. Third, try to avoid etching GaSb surfaces, as the oxide is not stable and there are limited options for selective etching. Fourth, switch to $In_xGa_{1-x}As_ySb_{1-y}$ as an absorber, or even $InAs_ySb_{1-y}$, as Indium based materials have much longer SRH lifetimes. The MWIR and LWIR detector communities have already begun their wholesale shift away from GaSb after two decades of research. And fifth, utilize delta-doping to limit the conduction band offsets, although only a fraction as much as the interface charge density.

2. Five Not-So-Easy Pieces

There are several research pursuits that can be identified from this dissertation that would be technologically useful. The first is the recombination velocity of the IMF isotype heterojunction in both forms (*p*-GaSb on *p*-GaAs and *n*-GaSb on *n*-GaAs). This information is needed to accurately model the internal quantum efficiency of photodiodes. The second is the use of lateral illumination (travelling-wave photodiodes) to determine the limiting bandwidth of carriers in GaSb photodiodes. Since GaAs has a lower permittivity than GaSb at most wavelengths, it should be possible to confine the optical mode in the GaSb region only. And a final pursuit is taking the lessons learned from GaAs and moving to silicon substrates. New problems will arise with silicon, including anti-phase domains, differences in the coefficient of thermal expansion, and thermal barriers. Research into the silicon IMF technique at UCLA indicated for the first time the role of epitaxial tilt, wafer curvature, and AlSb surface roughening in the material qualities, while the device properties remained unexplored. However, the basic goals of moving to larger, cheaper substrates with low noise multiplication regions will remain.